Journal of Medicinal Chemistry

Article

High Sensitive Near-Infrared Fluorophores for in Vivo Detection of Amyloid-# Plaques in Alzheimer's Disease

Hualong Fu, Mengchao Cui, Liu Zhao, Peiyu Tu, Kaixiang Zhou, Jiapei Dai, and Boli Liu

J. Med. Chem., **Just Accepted Manuscript** • DOI: 10.1021/acs.jmedchem.5b00861 • Publication Date (Web): 11 Aug 2015

Just Accepted

ACS Publications

Journal of Medicinal Chemistry is published by the American Chemical Society. 1155 Sixteenth Street N.W., Washington, DC 20036

High Sensitive Near-Infrared Fluorophores for in Vivo Detection of Amyloid-β Plaques in Alzheimer's Disease

Hualong Fu,[†] Mengchao Cui,[,†] Liu Zhao,[†] Peiyu Tu,[†] Kaixiang Zhou,[†] Jiapei Dai,[‡] and Boli Liu[†]*

[†]Key Laboratory of Radiopharmaceuticals, Ministry of Education, College of Chemistry, Beijing Normal University, Beijing 100875, P. R. China

[‡]Wuhan Institute for Neuroscience and Neuroengineering, South-Central University for Nationalities, Wuhan 430074, P. R. China

ABSTRACT

Alzheimer's disease (AD) is pathologically characterized by the accumulation of β-amyloid (Aβ) deposits in the parenchymal and cortical brain. In this article, we designed, synthesized and evaluated a series of near-infrared (NIR) probes with electron donor-acceptor end groups interacting through a π-conjugated system for the detection of Aβ deposits in the brain. Among these probes, **3b** and **3c** had excellent fluorescent properties (emission maxima > 650 nm and high quantum yields) and displayed high sensitivity and high affinities to Aβ aggregates (**3b**: K_d = 8.8 nM; **3c**: K_d = 1.9 nM). Both **3b** and **3c** could readily penetrate the blood-brain barrier with high initial brain uptake and fast to moderate washout from the brain. In vivo NIR imaging revealed that **3b** and **3c** could efficiently differentiate transgenic and wild-type mice. In summary, our research would provide new hints for developing smarter and more activatable NIR probes targeting Aβ.

INSTRUCTION

Alzheimer's disease (AD) stands out among the etiologies of acquired dementia and is becoming an extensive health problem with the ever-increasing aging population.[1, 2] Generally, it has been thought that the extracellular accumulation of β-amyloid (Aβ) peptides into plaques plays a vital role in AD onset.[3-5] Therefore, research on the development of probes for the in vivo detection of Aβ has emerged as a way to define the etiology of the dementia, deduce the progression of AD and provide an accurate index of putative anti-Aβ agents.

In the past decades, substantial research work has been dedicated to developing probes capable of crossing the blood-brain barrier (BBB) and selectively binding to Aβ plaques for use in structural imaging techniques, such as magnetic resonance imaging (MRI), positron emission tomography (PET) and optical imaging. MRI is a time-consuming tool in Aβ imaging due to the ambiguous signal contrast between amyloid plaques and surrounding tissue.[6, 7] To date, most radiolabeled small-molecule probes targeting Aβ have been developed for PET imaging, and three ^{18}F-labeled agents have been approved by the FDA;[8] however, the usage of short-lived isotopes requires an on-site cyclotron and a team of radiochemistry staff, limiting its widespread application.[8, 9] Optical imaging, including multiphoton microscopy and near-infrared (NIR) imaging, permits high temporal and spatial resolution. Furthermore, with the aid of fluorescence molecular tomographic (FMT) imaging, optical imaging has drawn more attention as an optimal tool in the detection and quantification of biological processes, preclinical trials, and drug development.[10-13] Multiphoton microscopy has been used for in vivo imaging in small animals and has served as a powerful approach to monitor the effects of anti-Aβ agents.[14] However, such microscopy is invasive and narrow-viewed, hence not applicable to the intact imaging of the brain compartment.[14, 15] NIR imaging, particularly relying on rationally designed NIR imaging agents (the NIR detection window is 650 - 900 nm), is a viable technique for non-invasive

imaging due to several advantages, such as sufficient light penetration depth in living tissues, avoidance of radiation, noninvasive operation, real-time imaging and inexpensive instruments.

Several NIR probes aimed at the early detection of AD have been reported to date (Figure. 1). AOI-987 is a charged molecule with a small Stocks shift (the wavelength value derived from the difference between excitation and emission of a fluorophore, 20 nm) and moderate affinity (K_d = 220 nM), which implies limited BBB permeability and obscured signal increase upon binding with Aβ plaques.[16] Better yet, Ran et al. have exploited curcumin derivatives as NIR probes for soluble or insoluble Aβ species. In 2009, CRANAD-2 was reported as a NIR probe for Aβ plaques with advantages over other candidates such as its ideal binding constant (K_d = 38.7 nM) and optimal fluorescent properties (emission maximum at 805 nm).[17] More recently, CRANAD-58 has been designed and synthesized for detecting both insoluble and soluble Aβ species in vitro and in vivo.[18] However, the slow brain washout rate caused by their high lipophilicity has impeded their application in NIR imaging. Additionally, BAP-1 with high quantum yield (QY) and high affinity to Aβ aggregates (K_d = 44.1 nM) was explored as another NIR probe targeting Aβ plaques, but the small Stocks shift (34 nm) and high nonspecific uptake in the scalp hindered its practical use for in vivo imaging.[19]

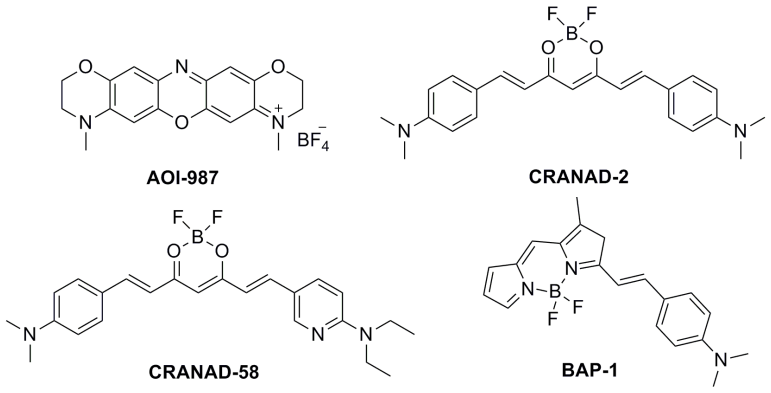

Figure 1. Structures of the reported NIR probes for detecting insoluble or soluble Aβ species.

RESULTS AND DISSCUSSION

Design, synthesis and fluorescent properties. To design feasible imaging probes for the in vivo detection of Aβ plaques in the brain, our group exploited the electron donor-acceptor (D-A) architecture as a preferable scaffold using the following rationale.[20, 21] 1) Due to the internal charge transfer (ICT) transition, these "D-A" molecules exhibit a striking discrepancy between dipole moments in their ground and lowest energy singlet excited states.[22] Extended π-conjugated systems could result in increased electronic delocalization, which induces a much narrower band gap between the excited and ground states, leading to an emission wavelength in the deep-red or NIR spectral range.[23-26] Our probes displayed reasonable fluorescent properties (moderate increase in fluorescence intensity upon binding to Aβ aggregates with a blue shift) and moderate to high affinities to Aβ aggregates, among which DANIR 2c (Figure 2) had the highest affinity (K_d = 26.9 nM). For NIR imaging, the spatial resolution is limited when probing through the intact cranium and scalp. Thus, the quantification of the amyloid plaques in the brain achieved by the spatial integration of fluorescence intensity mainly relies on the sufficient light penetration depth and the high QY of the fluorophore. Thus the low QY of our D-A probes impeded all their practical application in vivo. 2) Our previous work also suggested that the conjugated double-bond bridge was crucial for Aβ binding and that the affinity increased with the extension of the π-bridge.[20, 21] 3) As reported, for aromatic hydrocarbons such as benzene, naphthalene, anthracene and pyrene, a remarkable increase in QY was observed when the size increased from 1 to 4 rings.[27] Therefore, it is reasonable to speculate that the QY could be improved by replacing the benzene ring with a naphthalene ring. 4) Furthermore, 2-(1-(6-(dimethylamino)naphthalen-2-yl)ethylidene)malononitrile (DDNP, Figure 2) with a hydrophobic naphthalene ring was reported by Jacobson et al. as an environmentally sensitive, hydrophobic and neural fluorophore with high dipole moment for fluorescence microscopy that was capable

of readily passing cell membrane.[28] In 2012, the analogs of DDNP were explored by Petric et al. as probes for the neuroimaging of amyloids, and most of the probes displayed high affinities to Aβ aggregates.[29] Additionally, 2-(1-[6-[(2-fluoroethyl)(methyl)amino]-2-naphthyl]ethylidene) (FDDNP, Figure 2), a fluorinated DDNP version with a high affinity for A$\beta_{1\text{-}40}$ fibrils, has been reliably utilized for the histological staining of amyloid-like protein specimens and became the first PET imaging probe for the location of Aβ and neurofibrillary tangles (NFTs) in the brains of AD patients.[30, 31] However, the deficient emission wavelength has precluded their application as NIR probes. 5) Finally, the *N*,*N*'-dimethylamino group is an ideal electron donating moiety and an encouraging substituent for better Aβ binding affinity, and its planar geometry allows efficient conjugation with the naphthalene ring system.[29, 32, 33] Based on the above design rationale, we report the synthesis, characterization, and biological evaluation of a more extensive series of D-A molecules (DANIR **3a**-**e**, Figure 2) as NIR imaging probes for Aβ plaques in AD. The binding models of these probes to Aβ_{40} fibrils were explored by molecular docking simulation.

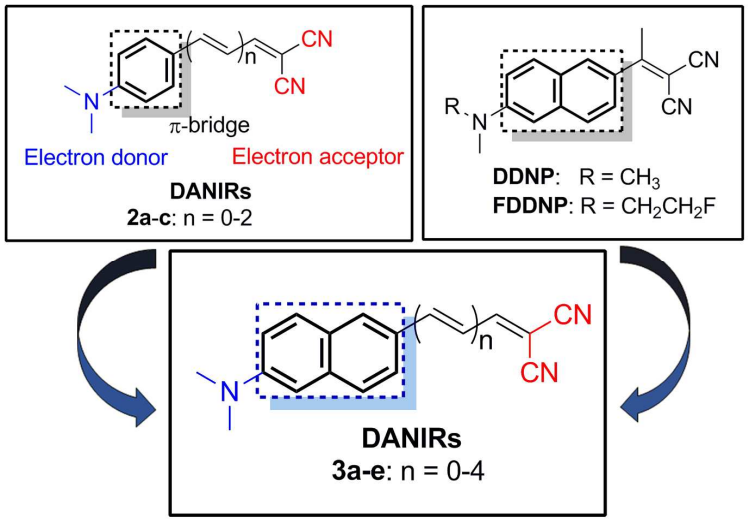

Figure 2. Chemical structures of DANIR 2a-c, DDNP, FDDNP and newly designed DANIR probes.

The synthesis of the newly designed DANIR probes is shown in Scheme 1. The Wittig reaction was employed to extend the polyenic chains in preparing naphthyl aldehydes. To obtain the final probes, the naphthyl aldehydes were subjected to the Knoevenagel reaction with malononitrile catalyzed by K_2CO_3, and most of the products (except **3e**) could be crystallized from the reaction mixture in good yields (> 70%). The single crystal structures of **3b** and **3c** were presented as ORTEPs (Figure 7), and relevant crystallographic data are listed in Table S5 in Supporting Information. In contrast to DDNP and its analogs,[28, 29] each of the probes crystallized into one planar conformer. Single-crystal structures and ^{1}H NMR data demonstrated that **3a**-**e** existed in the *E* isomer. The purity of **3a**-**e** was determined to be higher than 98% by high-performance liquid chromatography (HPLC).

As anticipated, with the lengthening of the polyenic chains, the probes showed significant bathochromic shifts of absorption/emission maxima and solvent dependency in various solvents, indicating a narrowing HOMO-LUMO gap and ongoing ICT transition (Figure S2 and S3, and Table S1 in Supporting Information).[28] As shown in Table 1, the emission wavelengths of **3b**-**e** red-shifted to the NIR range (> 680 nm in PBS) with large Stokes shifts (> 120 nm). Due to the longer polyenic chains, **3d** and **3e** exhibited emission wavelengths of 828 and 830 nm in PBS, respectively, which were longer than the emission wavelength of CRANAD-2. Furthermore, **3b** and **3c** exhibited high QYs of 29.9% and 9.0% in dichloromethane (DCM), respectively, considerably higher than the QY of DANIR 2c (4%). As shown in Figure S1 in Supporting Information, molecules presenting extended polyenic chains (**3d** and **3e**) displayed an onset of saturation of the excited state dipole (as well as the emission maxima). This result could be related to both charge delocalization and structural effects, which counterbalance the length effect. That is to say, the extension of the conjugated system results in increased photoinduced

charge delocalization, leading to tapering-off of the excited state dipole. Concurrently, multiple torsions along the single bonds of the polyenic chains could remarkably affect the global geometry of the molecules in solution, thus influencing the excited state dipole.[34] These effects also had a marked impact on the QYs of the probes. With increasing polyenic chain length, an intense decrease in QY was observed from **3b** to **3e** (Table 1 and Figure S1 in Supporting Information). As suggested by our results, lengthening the polyenic chains had a limited effect in achieving compounds with longer emission maxima and might produce undesirable results, including decreased QY. These results provide meaningful guidelines for the design of D-A based NIR probes.

Scheme 1.[a] Synthesis of naphthyl aldehydes and DANIR probes.

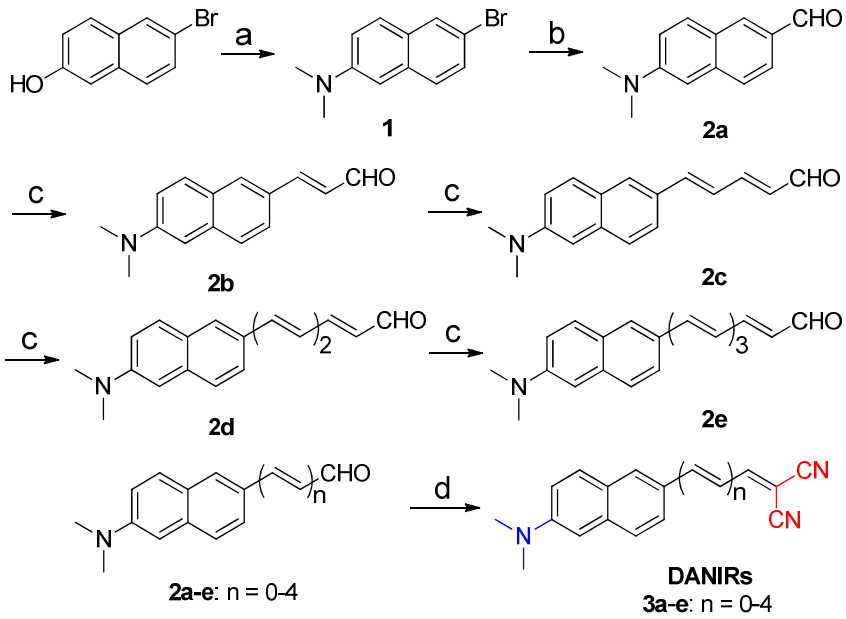

[a]Reagents and conditions: (a) Dimethylamine (33% in aqueous solution), $Na_2S_2O_5$, water, 140 °C, high pressure, 18 h. (b) (1) *n*-BuLi (2.5 M in hexane), anhydrous THF, -78 °C, 30 min, (2) anhydrous DMF, r.t, 15 min, (3) HCl (1 M), r.t. (c) (1) ((1,3-Dioxolan-2-yl)methyl)triphenylphosphonium bromide, anhydrous THF, NaH, 18-crown-6, r.t, 24 h; (2) HCl (1 M), r.t. (d) Malononitrile, K_2CO_3, methanol or THF, r.t, 5 min.

Table 1. Fluorescent properties, binding data and calculated log *P* (clog *P*) values of **3a**-**e**, DANIR 2c, CRANAD-2 and BAP-1.

Probe	λ_{em1} (nm) [a]	λ_{em2} (nm) [a]	Φ (%) [b]	Fold [c]	K_d (nM) [d]	K_i (nM) [d]	cLog P [k]
3a	614	538	4.8/0.1	331	44.8 ± 15.3	156.4 ± 15.8	3.46
3b	682	615	29.9/0.3	716	8.8 ± 1.5	96.7 ± 6.7	4.05
3c	783	678	9.0/0.009	280	1.9 ± 1.1	32.7 ± 3.4	4.56
3d	828	716[e]	3.7/0	5[e]	n/o	197.4 ± 43.3	5.10
3e	830	n/o	0.1/0	n/o	n/o	> 1000	5.62
DANIR 2c	665[f]	625[f]	4.1[f]/0.2[g]	12[f]	26.9[f]	36.9[f]	3.37
CRANAD-2	749[g]	n/o	70.3[g]/0.04[g]	n/o	-	-	6.16
	805[h]	715[h]	40[h,i]/0.6[h]	70[h]	38.69[h]	-	-
BAP-1	648[j]	648[j]	13.5[g]/0[g]	-	44.1[j]	-	3.52

[a]Determined in PBS (λ_{em1}) and upon binding with Aβ aggregates (λ_{em2}). [b]Measured in DCM/PBS, respectively. [c]Fold increase in fluorescence intensity upon binding with Aβ aggregates. [d]K_d and K_i values of **3a**-**e** were measured in triplicate with results given as the mean ± SD. [e]A solution of **3d** in PBS (30% ethanol, 1 μM) was used. [f]Data from ref.[21]. [g]Data were measured in the same conditions with **3a**-**e**. [h]Data from ref.[17]. [i]QY was measured after CRANAD-2 bound to Aβ_{40} aggregates. [j]Data from ref.[19]. [k]The values were calculated using the online ALOGPS 2.1 program. n/o: not observed.

In vitro characterizations. A valuable property of a fluorophore is its sensitivity to the surrounding environment, so an ideal Aβ probe should have a "turn-on" mechanism after binding to Aβ plaques. We first evaluated the fluorescence response of **3a**-**e** toward the synthetic A$\beta_{1\text{-}42}$ aggregates or bovine serum albumin (BSA) in PBS (pH = 7.4). As expected, in a solution containing Aβ aggregates, most of the probes (except **3d** and **3e**) exhibited a remarkable increase in fluorescence intensity (ranging from 280- to 716-fold) and significant blue shifts (ranging from 35 to 79 nm) at a low final concentration of 50 nM, whereas **3d** only showed a weak response (5-fold) at a high concentration of 1 μM (Table 1, Figure 3 and S4 in Supporting Information). Moreover, no significant changes in the fluorescence intensity and emission

wavelength were observed when **3e** and CRANAD-2 were incubated with Aβ aggregates in the experiment condition (Figure S4 in Supporting Information). The results also suggested that no interaction occurred between our probes and BSA. The "turn-on" phenomenon of **3a**-**d** toward Aβ aggregates occurs mainly because these small molecules have intercalated into the hydrophobic clefts of the aggregated amyloid fibrils with high affinities. This interpretation was further confirmed by the significant changes of the QYs in DCM and PBS, solvents with increasing polarity (Table 1). These results suggested that most of our probes have high sensitivity to Aβ aggregates and can be selectively "turned on" upon binding with them. Furthermore, the high sensitivity of **3a**-**c** in detecting Aβ aggregates paves the way for their potential application in fluorescence intensity distribution analysis during anti-Aβ drug screening, which plays a significant role as a future readout technology for miniaturized high-throughput screening.[35]

Various Aβ plaques ranging from diffuse to highly compacted (dense-core) have been proved to be responsible for the neuropathology of AD. Another form of plaques distributed in the walls of small arteries and arterioles within the leptomeninges and cortex play a central role in the onset of cerebral amyloid angiopathy (CAA).[36] The selective binding of **3a**-**e** to different forms of amyloid plaques was determined by neuropathological fluorescence staining experiments using 8-μm brain sections from double transgenic (Tg) mice and four different AD/CAA patients. As shown by the staining patterns of the brain slices from Tg mice (Figure 3A and B, and S5 in Supporting Information), the presence and distribution of the fluorescent spots stained by **3a**-**d** were observed to colocalize with the Aβ plaques stained with thioflavin-S (Th-S, a common dye for staining Aβ fibrils). After incubating the brain slices from AD patients with solutions of **3a**-**e**, different forms of Aβ plaques including diffuse plaques, dense-core plaques

and plaques accumulating along the vessel walls were stained clearly by **3a**-**d** with a high contrast-to-background fluorescence ratio (Figure 3C and D, and S6 in Supporting Information). However, **3e** displayed no specific staining of the plaques in the brain slices from Tg mice or AD/CAA patients. Based on the staining patterns, most of the new probes (**3a**-**d**) can bind selectively to Aβ plaques in sections from both Tg mice and AD/CAA patients with high sensitivity and clarity, indicating their superior affinities to Aβ aggregates.

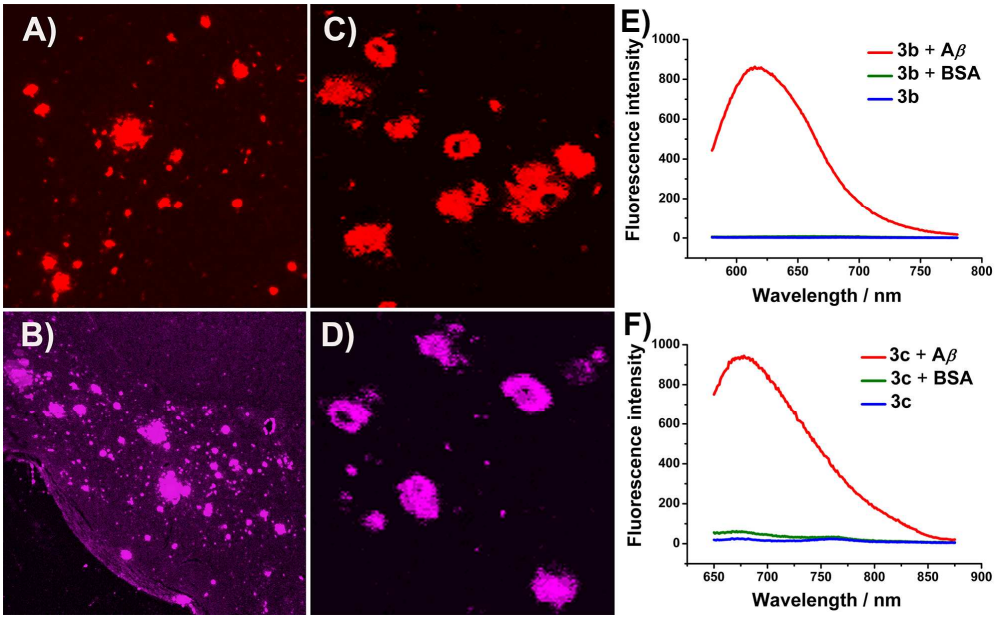

Figure 3. (A-D) Histological staining of brain slices from Tg mice (A and B, magnification: 10×) and an AD patient (C and D, magnification: 10×). A) and C), B) and D) were stained by **3b** and **3c**, respectively. (E and F) Emission wavelengths of **3b** (E) and **3c** (F) upon binding with Aβ aggregates or BSA.

The affinities of the probes for Aβ aggregates were quantitatively assessed through saturation and inhibition binding assays. Table 1 summarizes the K_d and K_i values of **3a**-**d**. In accordance with the Aβ aggregate binding and fluorescence staining results, **3a**-**d** displayed moderate to high affinities to A$\beta_{1\text{-}42}$ aggregates, whereas **3e** exhibited a poor affinity. It was found that **3a** had

comparable affinity (K_d = 44.8 nM) to CRANAD-2 (K_d = 38.7 nM) and DANIR 2c (K_d = 26.9 nM). More importantly, **3b** and **3c** exhibited very high affinities, with K_d values of 8.8 and 1.9 nM, respectively, higher than the values of all of the reported NIR Aβ probes. In the inhibition assays, most of the probes (except **3e**) inhibited [^{125}I]IMPY in a dose-dependent manner (Figure. S7D in Supporting Information). In both assays, the binding affinities of **3a**-**c** were improved with the lengthening of the π-bridge. It was previously extrapolated that a conjugated and planar architecture of a ligand is very important for Aβ binding, and small-size substitutions at the dicyanovinyl position could also improve the binding affinity.[8, 29] Each of these probes has a small-size hydrogen substitution at the dicyanovinyl position. Moreover, as proved by the crystal and optimized structures (Figure 7 and S17 in Supporting Information), the *N*,*N*'-dimethylnaphthalene and dicyanomethylene groups are approximately coplanar in the extended π-conjugated system. In our case, **3d** and **3e** had the longest polyenic chains, but conversely displayed decreased affinities to Aβ aggregates, mainly because the excessive torsions along the single bonds induced by prolonging the polyenic chain length blocked their ready access to the Aβ fibrils. Taken together, our probes exhibited high to poor affinities to Aβ aggregates. Notably, **3b** and **3c** had very high affinities, highlighting their potential application as NIR imaging probes in detecting and quantifying amyloid deposits within the tissue targets.

Biostability and BBB penetration. As the stability of the chemical entities in plasma is a prerequisite for showing good in vivo efficacy, we examined the stability of **3b** and **3c** in mice plasma. The results showed that the tested probes were stable with purities higher than 94% after incubation with mice plasma for 30/60 min (Figure S8 in Supporting Information), indicating that **3b** and **3c** had excellent biostability in plasma and could be developed for in vivo use.

The lipophilicity (log *P* within 1-3.5 range) and molecular weight (< 600 Da) of the ligands are two primary factors affecting the capability of BBB penetration. The molecular weights (M. W.) and calculated log *P* (clog *P*) values of **3b** (M. W. = 273.33, clog *P* = 4.05) and **3c** (M. W. = 299.37, clog *P* = 4.56) were lower than for CRANAD-2 (M. W. = 410.26, clog *P* = 6.16) and a little higher than for DANIR 2c (M. W. = 249.31, clog *P* = 3.37). This result indicates that **3b** and **3c** have great potential in BBB penetration. The brain uptake of **3b** and **3c** was intuitively confirmed by dissecting brain samples at 2 min after intravenous (i.v.) injection of the probes (Figure 4A). Under visible light, the brain dosed with **3b** appeared in darker color than the control brain. Due to the high QY and brain uptake of **3b**, the corresponding brain appeared shiny red under ultraviolet (UV) light (365 nm). The BBB penetrating ability of our probes was quantified in ICR mice, and the data were expressed as the percent injected dose per gram of tissue (% ID/g). As shown in Table 2, **3b** displayed high initial brain uptake at 2 min (12.80 % ID/g) and fast washout from the brain at 60 min post-injection ($brain_{2\ min}/brain_{60\ min}$ = 21.3), vital qualities in achieving a preferable signal-to-noise ratio. Due to higher lipophilicity and larger molecular weight, **3c** showed decreased brain uptake (4.44 % ID/g at 10 min post-injection) and slower washout from the brain ($brain_{10\ min}/brain_{60\ min}$ = 3.3), whereas **3d** and **3e** could not penetrate the BBB. Determined in the same conditions, DANIR 2c could rapidly penetrate into the brain with high initial uptake (16.88 % ID/g at 2 min post-injection), and wash out from the brain very fast ($brain_{2\ min}/brain_{60\ min}$ = 42.2). In accordance with the NIR imaging results,[17] CRANAD-2 displayed slow washout from the brain ($brain_{10\ min}/brain_{60\ min}$ = 2.4). BAP-1 displayed low brain uptake (2.37 % ID/g at 10 min post-injection), slow egress from the brain ($brain_{10\ min}/brain_{60\ min}$ = 5.5), and significant instability in the living brain.[20] As seen from the HPLC profiles (Figure S10 in Supporting Information), **3b** showed excellent biostability, while

3c was metabolized as of 10 min post-injection. The experimental log *P* values and kinetics of **3b** and **3c** in the blood of mice has been evaluated. As shown in Table 3, the experimental log *P* values were unanimous to the calculated ones (Table 1). Both **3b** and **3c** showed fast clearance from the blood. Furthermore, **3c** displayed considerably higher lipophilicity and initial uptake in blood (log *P* = 4.48, $blood_{2\ min}$ = 3.40 % ID/g) than for **3b** (log *P* = 4.10, $blood_{2\ min}$ = 1.90 % ID/g), which may account for the lower brain uptake of **3c**. In summary, the length of the polyenic chains had a significant impact on the brain kinetics of the probes and the extension of the polyenic chains clearly decreased the initial brain uptake and brain washout rate. Of note, **3b** displayed rapid penetration through the intact BBB, fast washout from the brain and excellent biostability in the living brain, demonstrating that **3b** is a promising Aβ probe for in vivo NIR imaging.

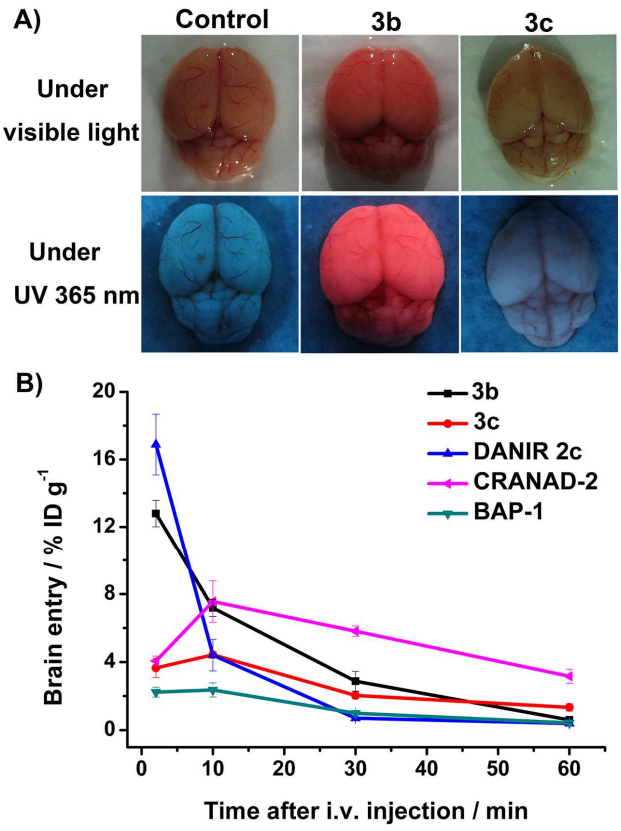

Figure 4. (A) Brains of ICR mice separated at 2 min after i.v. injection of **3b** and **3c** under visible light (top row) and UV light (365 nm, bottom row). Brains were also dissected from mice directly as a control. (B) Comparison of brain uptake of **3b**, **3c**, DANIR 2c, CRANAD-2 and BAP-1 in ICR mice.

Table 2. Brain kinetics of **3b**, **3c**, DANIR 2c, CRANAD-2 and BAP-1 in ICR mice.

Probe	Time after injection / % ID/g				$Brain_{10\ min}/brain_{60\ min}$
	2 min	10 min	30 min	60 min	
3b	12.80 ± 0.78	7.18 ± 0.50	2.88 ± 0.58	0.60 ± 0.15	21.3[a]
3c	3.65 ± 0.56	4.44 ± 0.20	2.05 ± 0.20	1.34 ± 0.22	3.3
DANIR 2c	16.88 ± 1.80	4.41 ± 0.92	0.70 ± 0.02	0.40 ± 0.05	42.2[a]
CRANAD-2	4.06 ± 0.28	7.56 ± 1.22	5.82 ± 0.31	3.17 ± 0.42	2.4
BAP-1[b]	2.23 ± 0.29	2.37 ± 0.42	1.00 ± 0.15	0.43 ± 0.07	5.5

[a]The clearance rate of **3b** and DANIR 2c are presented as $brain_{2\ min}/brain_{60\ min}$. [b]Data from ref.[20].

Table 3. The experimental log *P* values and blood clearance rate of **3b** and **3c** in ICR mice.

Probe	Log *P*	Time after injection / % ID/g	
		2 min	60 min
3b	4.10 ± 0.17	1.90 ± 0.12	0.25 ± 0.010
3c	4.48 ± 0.0045	3.40 ± 0.52	0.065 ± 0.0027

In vivo imaging and ex vivo fluorescence staining. To validate the feasibility of **3b** and **3c** for in vivo NIR imaging, nude mice were i.v. injected with the probes to observe the brain kinetics. As shown in Figure S11 and S12 in Supporting Information, nearly all of the fluorescence signals were centralized in the brain compartments and could be captured

efficiently, indicating that **3b** and **3c** can readily penetrate into the BBB and have potential applications for in vivo NIR imaging of the brain compartment. In accordance with the brain kinetics results, the brain egress of **3b** was much faster than for **3c**.

Next, to confirm the great potential of **3b** and **3c** in non-intrusively detecting Aβ plaques in the brain, we performed in vivo NIR imaging with Tg mice and age-matched wild-type (WT) mice. Semi-quantitative information was obtained from the recorded images at different time points before and after dye dosing following equation (1). As shown in Figure 5A, the fluorescence signals of **3b** displayed striking differences between the Tg and WT groups at the earliest time point of 10 min after i.v. administration, earlier than for CRANAD-2 and AOI987 (t = 30 min). Furthermore, as shown in Figure 5B, the fluorescence signals of **3b** in the brains of Tg mice decreased at a considerably slower rate, and the discrepancies of the fluorescence signals between the Tg and WT mice [F(Tg)/F(WT) ranged from 1.0 to 2.1] became larger in the course of the detection time (0 - 60 min), indicative of specific dye retention trapping by amyloid plaques. However, due to its inadequate brain uptake, slow brain washout rate and instability in living brains, **3c** showed fluorescence signal differences between the Tg and WT groups at a hysteretic time point of 30 min, and narrower discrepancies of the fluorescence signals [F(Tg)/F(WT) ranging from 1.0 to 1.5] were observed (Figure 5C and D). In consideration of the blue-shift of the probes after binding to the Aβ plaques, the fluorescent light emitted at shorter wavelengths (620 and 680 nm for **3b** and **3c**, respectively) from the mice brains was also detected. As shown in Figure S13 and S14 in Supporting Information, the fluorescence signals of **3b** at 620 nm displayed significant differences between the Tg and control groups from 10 min post injection, with large discrepancies [F(Tg)/F(WT) ranging from 1.0 to 2.8]. However, for the captured fluorescence behaviour of **3c**, no noteworthy differences were obtained between the

results under 780 and 680 nm. In conclusion, due to the high QY, excellent brain kinetics and biostability, **3b** presented advantages over **3c** in in vivo NIR imaging and exhibited great capacity to distinguish Tg and WT mice.

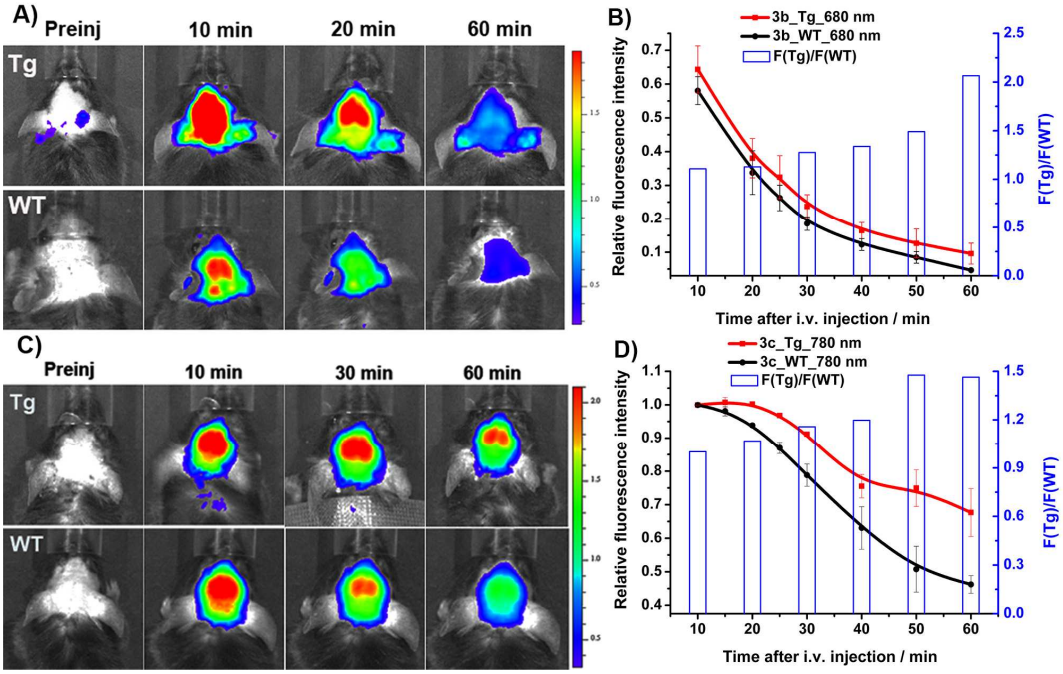

Figure 5. In vivo imaging of Aβ deposits by **3b** and **3c**. (A and C) Representative images of Tg mice (top row) and age-matched WT ones (bottom row) at selected time points before and after i.v. injection of **3b** (A) and **3c** (C). (B and D) Relative fluorescence intensity in the brain compartments of Tg mice (red line) and WT mice (black line) after i.v. injection of **3b** (B) and **3c** (D). The differences of the fluorescence signals between Tg and WT mice were also illustrated by the values of F(Tg)/F(WT) (right Y axis). The fluorescence signals of **3b** and **3c** were recorded at 680 (A and B) and 780 nm (C and D), respectively.

The in vivo imaging results were further confirmed by ex vivo fluorescence staining of frozen brain sections from Tg and WT mice after administration of **3b** and **3c**. Under fluorescence microscopy, Aβ plaques were observed in the cortex (Figure 6) and cerebellum (Figure S15 in

Supporting Information) regions after in vivo staining by **3b** and **3c**, respectively, whereas the sections of WT mice showed no such fluorescent spots (Figure S16 in Supporting Information). In addition, the distribution of the amyloid plaques was confirmed by staining the same sections with Th-S (Figure S15 in Supporting Information). This result confirmed that **3b** and **3c** could specifically label the amyloid plaques in vivo; hence, the discrepancies of the fluorescence signals between the Tg and WT mice in NIR imaging were due to the specific retention of the probes after binding to the Aβ plaques.

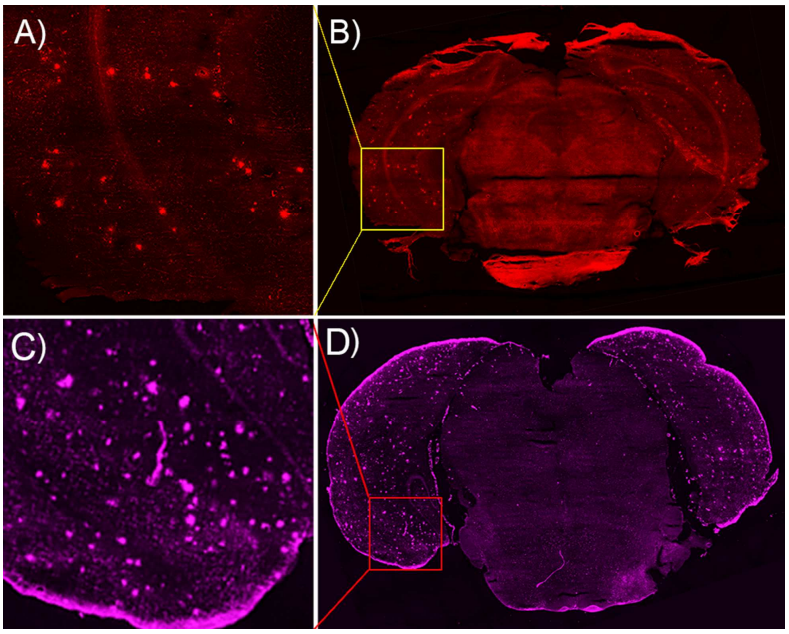

Figure 6. Ex vivo histology results of brain slices of cortex regions of Tg mice after dosing with **3b** (A and B) and **3c** (E and F). (A) and (C) are partial enlarged views of homologous sections. Magnification: 10×.

Computational studies. Computational approaches have been widely used in studying protein-ligand interactions, including their applications in exploring the binding modes and interactions of probes such as thioflavin-T (Th-T),[37] Congo Red (CR),[38, 39] $[Ru(bpy)_2dppz]^{2+}$[40] and benzyloxybenzene derivatives[41] toward Aβ. In this study, the binding modes of **3a**-**e** to Aβ

fibrils were examined by molecular docking simulations. The lowest-energy/top-ranked docking poses are shown in Figure 7: **3a**-**e** bound to the grooves on the KLVFFA fibril surface, an identical binding site to CR[39] and IMPY[41], namely, a hydrophobic cleft oriented parallel to the main fibril axis formed by VAL18 and PHE20. Considering that the mature amyloid fibrils have lengths > 1 μm,[42] the long grooves on the amyloid fibril surface are ubiquitous. We could extrapolate that this binding site is a general recognition mode of amyloid fibrils by planar molecules.[39, 40] Analysis of the docking results showed that the molecules with larger conjugated systems and dipole moments could better fit the binding channel with lower binding energies (Table S6 in Supporting Information); concurrently, for **3a**-**c**, a good correlation between the pK_i values and binding energies (R^2 = 0.92) was observed. However, the K_i values (binding affinities) of **3d** and **3e** did not coincide well with the computational binding energy. A more detailed discussion about the docking results can be found in Supporting Information. Therefore, our computational studies could partially reproduce our experimental trends and suggested that **3a**-**e** likely filled in the grooves on the fibril surface formed by VAL18 and PHE20 with valid shape complementarities.

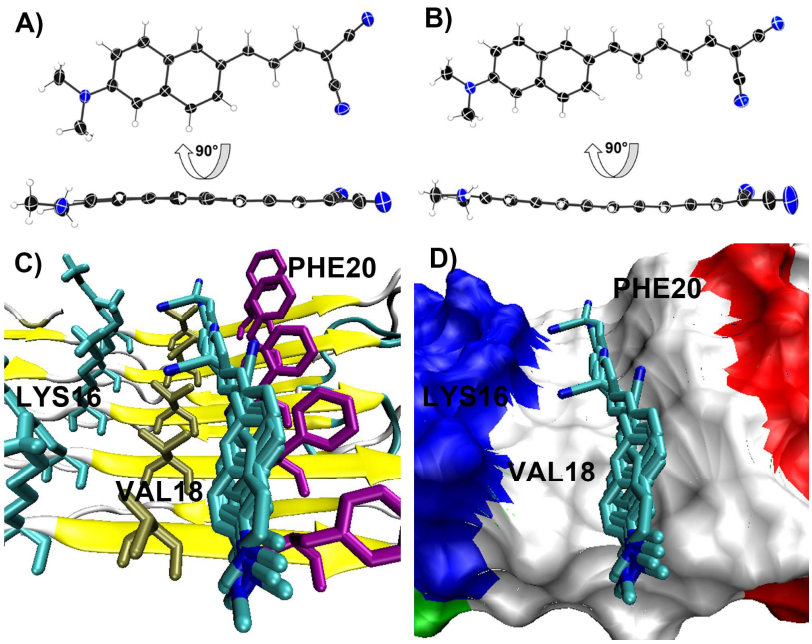

Figure 7. ORTEP structures of **3b** (A) and **3c** (B) and merged docking conformations of **3a**-**e** (C and D). The residues of Aβ fibrils are presented in the licorice style (C) and a molecule surface representation (D).

CONCLUSIONS

In this report, we successfully designed and synthesized a new family of DANIR probes (**3a**-**e**) with electron donor-acceptor architecture for the detection of Aβ plaques for NIR imaging. Most of these probes (**3a**-**c**) could be "turned on" by Aβ aggregates with high sensitivity and remarkable fluorescent property changes. The DANIR probes possess various affinities to Aβ aggregates. Among them, **3b** and **3c** exhibit the highest affinities and meet all of the requirements of a NIR probe for detecting Aβ deposits noninvasively in vivo.[17, 21] Our results also demonstrated that polyenic chains (C=C bonds) have a significant impact on the characteristics of the probe, such as the fluorescent properties, affinity and brain kinetics. Increasingly, fluorescent imaging has been used for drug discovery because of the simple

operation, short acquisition time and simultaneous measurement of several mice, compared with the much longer data acquisition time on a single animal by PET, SPECT or MRI.[43] Thus, the application of **3b** and **3c** could accelerate the throughput and development of anti-Aβ drugs. The binding modes of **3a**-**e** with Aβ fibrils were extensively studied with docking simulations and the results suggested that our probes most likely bound to the clefts on the surface of the Aβ fibrils. In summary, we designed and synthesized a series of NIR probes capable of sensing Aβ aggregation/plaques in vitro or in vivo and our results could shed light on developing a new generation of smarter and more activatable NIR probes targeting Aβ.

EXPERIMENTAL SECTION

General Information. All chemicals were commercial products of analytical grade, and were used without further purification unless otherwise indicated. Column chromatography purification was performed on silica gel (Yantai Industry Research Institute, 80 - 100 Å) packed into glass columns. The synthetic trifluoroacetic acid salt forms of amyloid-β (1-42) peptides were obtained from Osaka PEPTIDE INSTITUTE, Inc. (Osaka, Japan), and aggregated for in vitro studies using the previously reported procedures.[44] ^{1}H and ^{13}C NMR were obtained at 400 MHz and 100 MHz, respectively, on a Bruker spectrometer in $CDCl_3$ solutions at room temperature, and the chemical shifts were quoted in δ values (parts per million, ppm) downfield relative to the internal TMS. Mass spectra and the high-resolution mass were acquired using a Surveyor MSQ Plus (ESI) instrument and a GCT CA127 Micronass UK instrument.

Fluorescence and ultraviolet-visible spectra were measured using a spectrofluorophotometer (RF-5301PC, Shimadzu, Japan) and a UV spectrophotometer (UV-2450, Shimadzu, Japan), respectively. Fluorescence QYs were measured using an aqueous solution of Rhodamine 6G as a

standard (Φ = 0.76).[45] The purity and biostability in mice plasma of the key compounds were determined by HPLC performed on a Shimadzu SCL-20 AVP system equipped with a SPD-20A UV detector (λ = 254 nm). The HPLC analysis was performed on a Venusil MP C18 reverse phase column (Agela Technologies, 5 μm, 4.6 mm × 250 mm). In the BBB penetration test, an Agilent 1260 Infinity Quaternary LC (Agilent Technologies) system was used, and the HPLC analyses were performed on a Cosmosil packed column (5C18-AR-II, 4.6 × 150 mm, Nacalai Tesque). In the HPLC analyses, a binary gradient elution system was used, where the mobile phases A and B were water and acetonitrile, respectively. Fluorescence observation was performed on the Axio Observer Z1 (Zeiss, Germany) equipped with DAPI, AF488, AF546 and Cy 5.0 filter sets. Human brain sections of AD/CAA patients were obtained from Chinese Brain Bank Center.

Normal ICR mice (5 weeks, male) were used for BBB penetration determination and normal nude mice (BALB/c nude, 6 weeks, female) were used for in vivo imaging (purchased from Vital River Laboratory Animal Technology Co. Ltd., Beijing, China). Tg mice (C57BL6, APPswe/PSEN1, 14-19 months old, female), used as Alzheimer's models, were purchased from the Institute of Laboratory Animal Science, Chinese Academy of Medical Sciences. All animal experiments were approved by the animal care committee of Beijing Normal University.

Chemistry. **6-Bromo-*N*,*N*-dimethylnaphthalen-2-amine** (**1**) Compound **1** was prepared by a previously reported procedure[29] and a white solid (4.43 g, 65.8%) was obtained.

6-(Dimethylamino)-2-naphthaldehyde (**2a**) Compound **2a** was prepared by a previously reported procedure[29] and a yellow solid (8.6 g, 93.5%) was obtained.

(*E*)-3-(6-(Dimethylamino)naphthalen-2-yl)acrylaldehyde (**2b**) To a stirred solution of **2a** (1.5 g, 7.5 mmol) in anhydrous THF (25 mL) was added (1,3-dioxolan-2-

ylmethyl)triphenylphosphonium bromide (5.7 g, 13.2 mmol). NaH (60% dispersion in mineral oil, 1.7 g) was then added to the suspension in small portions, after which 18-crown-6 was added as catalyst. The stirring was continued for 24 h at room temperature, and then the reaction was quenched with an aqueous solution of HCl (1 M), followed by neutralization with ammonia water. The mixture was extracted with CH_2Cl_2 (3×40 mL), and the organic phase was dried over anhydrous magnesium sulfate. After the solvent was removed in vacuum, the residue was purified by flash column chromatography (petroleum ether/CH_2Cl_2/ ethyl acetate = 6:6:1, v: v) to give compound **3** as a yellow solid (770 mg, 45.4%). mp 145.3-146.6 ℃. ^{1}H NMR (400 MHz, $CDCl_3$) δ: 9.71 (d, *J* = 7.8 Hz, 1H), 7.84 (s, 1H), 7.77 (d, *J* = 9.0 Hz, 1H), 7.67 (d, *J* = 8.6 Hz, 1H), 7.58 (d, *J* = 16.0 Hz, 1H), 7.57 (d, *J* = 9.0 Hz, 1H), 7.22 (d, *J* = 8.4 Hz, 1H), 7.00 (s, 1H), 6.75 (dd, *J* = 15.8 Hz, 7.8 Hz, 1H), 3.12 (s, 6H). MS: m/z calcd for $[C_{15}H_{15}NO + H]^+$ 226.1, found 226.2.

(2*E*,4*E*)-5-(6-(Dimethylamino)naphthalen-2-yl)penta-2,4-dienal (**2c**) The same reaction described above to prepare compound **2b** was used, and the brown solid **2c** was obtained (83.0 mg, 33.5%). mp 192.8-193.7 ℃. ^{1}H NMR (400 MHz, $CDCl_3$) δ: 9.61 (d, *J* = 8.0 Hz, 1H), 7.73 (s, 1H), 7.70 (d, *J* = 9.1 Hz, 1H), 7.62 (d, *J* = 8.6 Hz, 1H), 7.57 (d, *J* = 8.7 Hz, 1H), 7.30 (dd, *J* = 15.0 Hz, 10.6 Hz, 1H), 7.15 (d, *J* = 7.8 Hz, 1H), 7.12 (d, *J* = 15.3 Hz, 1H), 7.02 (dd, *J* = 15.3 Hz, 10.6 Hz, 1H), 6.89 (s, 1H), 6.26 (dd, *J* = 15.0 Hz, 8.0 Hz, 1H), 3.09 (s, 6H). MS: m/z calcd for $[C_{17}H_{17}NO + H]^+$ 252.1, found 252.1.

(2*E*,4*E*,6*E*)-7-(6-(Dimethylamino)naphthalen-2-yl)hepta-2,4,6-trienal (**2d**) The same reaction described above to prepare compound **2b** was used, and the dark red solid **2d** was obtained (140.0 mg, 25.3%). mp 213.8-214.2 ℃. ^{1}H NMR (400 MHz, $CDCl_3$) δ: 9.58 (d, *J* = 8.0 Hz, 1H), 7.68 (d, *J* = 9.5 Hz,1H), 7.67 (s, 1H), 7.61 (d, *J* = 8.6 Hz, 1H), 7.54 (d, *J* = 8.7 Hz, 1H),

7.20 (dd, *J* = 15.1 Hz, 11.3 Hz, 1H), 7.14 (d, *J* = 8.2 Hz, 1H), 6.95-6.85 (m, 4H), 6.55 (dd, *J* = 13.9 Hz, 11.4 Hz, 1H), 6.18 (dd, *J* = 15.1 Hz, 8.0 Hz, 1H), 3.08 (s, 6H). MS: m/z calcd for $[C_{19}H_{19}NO + H]^+$ 278.2, found 278.1.

(2*E*,4*E*,6*E*,8*E*)-9-(6-(Dimethylamino)naphthalen-2-yl)nona-2,4,6,8-tetraenal (**2e**) The same reaction described above to prepare compound **2b** was used, and the black solid **2e** was obtained (30.0 mg, 36.7%). mp 172.1-173.2 ºC. ^{1}H NMR (400 MHz, $CDCl_3$) δ: 9.57 (d, *J* = 8.0 Hz, 1H), 7.69 (d, *J* = 8.4 Hz,1H), 7.65 (s, 1H), 7.62 (d, *J* = 7.9 Hz, 1H), 7.55 (d, *J* = 8.6 Hz, 1H), 7.16 (dd, *J* = 15.1 Hz, 11.4 Hz, 1H), 6.97-6.67 (m, 5H), 6.47 (d, *J* =14.6 Hz, 1H), 6.48-6.42 (m, 1H), 6.16 (dd, *J* = 15.1 Hz, 8.0 Hz, 1H), 3.08 (s, 6H). MS: m/z calcd for $[C_{21}H_{21}NO + H]^+$ 304.2, found 304.0.

General procedure for Knoevenagel condensation: To a solution of naphthyl aldehyde in methanol (**2a**-**d**) or THF (**2e**) was added an excess of malononitrile (2 equiv), and then a solution of K_2CO_3 in methanol (100 μL) was added as catalyst. Precipitation of **3a**-**d** was achieved after stirring at r.t. for 5 min, and the precipitate was collected by filtration; **3e** was obtained by flash a column chromatography.

2-((6-(Dimethylamino)naphthalen-2-yl)methylene)malononitrile (**3a**) Compared with the reported procedure,[29] **3a** was prepared in a much faster (5 min versus 2 h), environmentally friendly (changed the reaction solvent pyridine with methanol) and straightforward (the product crystallized from the reaction mixture versus isolated by chromatography and re-crystallization) synthesis route in a higher yield (85.5% versus 76%) as a red solid. mp 203.0-204.3 ºC (literature 29: 211.0-214.5 ºC). ^{1}H NMR (400 MHz, $CDCl_3$) δ: 8.08 (d, *J* = 1.4 Hz, 1H), 7.96 (dd, *J* = 8.9 Hz, 1.9 Hz, 1H), 7.77 (d, *J* = 9.2 Hz, 1H), 7.70 (s, 1H), 7.63 (d, *J* = 8.8 Hz, 1H), 7.17 (dd, *J* = 9.2

Hz, 2.6 Hz, 1H), 6.85 (d, *J* = 2.4 Hz, 1H), 3.17 (s, 6H). MS: m/z calcd for $[C_{16}H_{13}N_3 + H]^+$ 248.1, found 248.0.

(*E*)-2-(3-(6-(Dimethylamino)naphthalen-2-yl)allylidene)malononitrile (**3b**) A dark red solid was obtained, yield 75.0%. mp 191.7-192.9 ºC. ^{1}H NMR (400 MHz, $CDCl_3$) δ: 7.82 (s, 1H), 7.73 (d, *J* = 9.1 Hz, 1H), 7.55-7.64 (m, 3H), 7.34 (dd, *J* = 15.0 Hz, 2.6 Hz, 1H), 7.20-7.26 (m, 1H), 7.16 (dd, *J* = 9.1 Hz, 2.4 Hz, 1H), 6.87 (s, 1H), 3.13 (s, 6H). ^{13}C NMR (100 MHz, $CDCl_3$) δ: 160.15, 151.34, 150.29, 137.29, 132.36, 130.36, 127.50, 127.19, 125.78, 124.21, 119.90, 116.35, 114.35, 112.46, 105.69, 79.26, 40.35. HRMS: m/z calcd for $C_{18}H_{15}N_3$ 273.1266, found 273.1270.

2-((2*E*,4*E*)-5-(6-(Dimethylamino)naphthalen-2-yl)penta-2,4-dien-1-ylidene)malononitrile (**3c**) A black solid was obtained, yield 93.3%. mp 240.0-240.9 ºC. ^{1}H NMR (400 MHz, $CDCl_3$) δ: 7.73 (s, 1H), 7.70 (d, *J* = 9.1 Hz, 1H), 7.61 (d, *J* = 8.5 Hz, 1H), 7.56 (d, *J* = 8.6 Hz, 1H), 7.46 (d, *J* = 11.9 Hz, 1H), 7.15-7.07 (m, 3H), 7.00 (dd, *J* = 15.0 Hz, 11.0 Hz, 1H), 6.87 (s, 1H), 6.81-6.75 (m, 1H), 3.11 (s, 6H). ^{13}C NMR (100 MHz, $CDCl_3$) δ: 159.42, 151.19, 149.68, 146.00, 136.33, 130.08, 129.86, 129.71, 127.07, 124.80, 124.71, 123.94, 119.99, 116.41, 114.31, 112.32, 105.80, 79.78, 40.54. HRMS: m/z calcd for $C_{20}H_{17}N_3$ 299.1422, found 299.1426.

2-((2*E*,4*E*,6*E*)-7-(6-(Dimethylamino)naphthalen-2-yl)hepta-2,4,6-trien-1-ylidene)malononitrile (**3d**) A black solid was obtained, yield 74.0%. mp 226.4-227.2 ºC. ^{1}H NMR (400 MHz, $CDCl_3$) δ: 7.71 (d, *J* = 8.2 Hz, 1H), 7.70 (s, 1H), 7.64 (d, *J* = 7.9 Hz, 1H), 7.57 (d, *J* = 8.2 Hz, 1H), 7.44 (d, *J* = 11.9 Hz, 1H), 7.20-7.17 (m, 1H), 7.03-6.85 (m, 5H), 6.72 (dd, *J* = 14.1 Hz, 12.0 Hz, 1H), 6.52 (dd, *J* = 13.5 Hz, 11.7 Hz, 1H), 3.11 (s, 6H). HRMS: m/z calcd for $[C_{22}H_{19}N_3 + H]^+$ 326.1652, found 326.1659.

2-((2*E*,4*E*,6*E*,8*E*)-9-(6-(Dimethylamino)naphthalen-2-yl)nona-2,4,6,8-tetraen-1-ylidene)malononitrile (**3e**) After the solvent was removed, the residue was purified by flash

column chromatography (petroleum ether/CH_2Cl_2/ethyl acetate = 10: 10: 1, v: v) to give compound **3e** as a black solid (5.0 mg, 29.0%). mp 234.3-235.2 ºC. ^{1}H NMR (400 MHz, $CDCl_3$) δ: 7.85-7.70 (m, 4H), 7.60 (s, 1H), 7.43 (d, *J* = 11.9 Hz, 1H), 7.00 (d, *J* = 14.1 Hz, 1H), 6.97 (d, *J* = 14.1 Hz, 1H), 6.90 (s, 1H), 6.86-6.68 (m, 4H), 6.55-6.44 (m, 2H), 3.13 (s, 6H). HRMS: m/z calcd for $[C_{24}H_{21}N_3 + H]^+$ 352.1808, found 352.1821.

X-ray Crystallography.10 mg of **3b** and **3c** were dissolved in 2 mL of DCM, respectively, and then 0.5 mL petroleum ether was slowly added. Upon gentle evaporation at room temperature, red (**3b**) or dark red (**3c**) crystals were yielded. The X-ray single-crystal structures were determined on a Rigaku R-AXIS RAPID IP XRD system with a Saturn724+ charge-coupled device (CCD) detector. Diffractometer at 153(2) K with graphite monochromated Mo Kα radiation (λ = 0.71073 Å) was used. All structures were solved using SHELXL-97 program[46] and refined with full-matrix least-squares on F^2 method. All the hydrogen atoms were geometrically fixed using the riding model.

Fluorescence Spectral Assessment of 3a-e with A$\beta_{1\text{-}42}$ and BSA. To the solutions of DANIR probes (50 nM) in 3 mL PBS (pH = 7.4) was added 140 μL suspension of the A$\beta_{1\text{-}42}$ aggregate in deionized water (for a final Aβ concentration of 10 μg/mL) or 100 μL solution of BSA in PBS (0.3 mg/mL, for a final concentration of 10 μg/mL). The mixture was incubated at 37 °C with slight and constant shaking (100 r/min) for 1.5 h. Then, the mixture was transferred to a quartz sampling cell and its fluorescence spectra were recorded by a RF-5301PC fluorescence spectrophotometer. The spectra of **3a**-**e** in PBS and of PBS buffer (as a blank control) were also measured using the same parameters. The final spectra were corrected using the blank control. For the characterization of **3d** and **3e**, a solution of 1 μM in PBS (30% ethanol) was used. CRANAD-2 (50 nM) was also measured in the same conditions.

In Vitro Histological Staining of Brain Slices of Tg Mice and Human Brain. Paraffin-embedded 8-μm brain tissue sections from double Tg mice (C57BL6, APPswe/PSEN1, 22 months old, male), three AD patients [female, 64 years old (F64), male, 91 years old (M91) and female, 71 years old (F71)] and a CAA patient [female, 68 years old (F68)] were used for in vitro fluorescence staining. Before use, the slices were well deparaffinized by washing with ethanol for 5 min after a 15-min immersion in xylene. The slices were incubated in aqueous solutions of **3a**-**e** (1 μM, 2.5% DMSO, 10% ethanol) for 10 min at room temperature and then washed with ethanol/water (v: v, 40%: 60%). Next, the brain sections were covered with cover glasses prior to fluorescence observation using an Axio Observer Z1 (Zeiss, Germany) equipped with DAPI, AF488, AF546, and Cy 5.0 filter sets. To confirm the substantial staining of the plaques, the adjacent sections of Tg mice were stained with Th-S (0.125 % aqueous solution).

In Vitro Aβ Aggregates Binding Constant Determination. A suspension of 100 μL A$\beta_{1\text{-}42}$ aggregates (1.6 μg per borosilicate glass tube) was added to a mixture containing 100 μL **3a**-**e** (500 to 0.0051 nM in the final assay mixture) and 800 μL of PBS (pH = 7.4) in a final volume of 1.0 mL. Nonspecific assays were defined without test probes. All assay mixtures were incubated at 37 °C with slight and constant shaking (100 r/min) for 1.5 h. Next, the solutions were transferred to black 96-well Costar assay plates, and the fluorescence intensity was measured using a fully equipped POLARstar Omega microplate reader (BMG LABTECH, Germany). Fluorescence intensity values of each probe were plotted versus their concentrations (Figure S7 in Supporting Information), and the binding constants were calculated using GraphPad Prism 5.0.

In Vitro Inhibition Binding Studies Using A$\beta_{1\text{–}42}$ Aggregates. Inhibition experiments were conducted in 12 × 75 mm borosilicate glass tubes according to the previously described

procedures with certain modifications.[47] Briefly, 100 μL of Aβ aggregates (86 nM in the final assay mixture) was added to a mixture containing 100 μL of radioligand [^{125}I]IMPY (140000 cpm/100 μL), 100 μL inhibitors (**3a**-**e**, 10^{-5} to $10^{-10.5}$ M in ethanol), and 700 μL 0.05% BSA aqueous solution in a total volume of 1.0 mL. The mixture was incubated for 2 h at 37°C, and then the bound and free radioactive fractions were separated by vacuum filtration through borosilicate glass fiber filters (Whatman GF/B) using a M-24 cell harvester (Brandel, Gaithersburg, MD). The radioactivity from filters containing the bound 125I ligand was determined in a γ-counter (Wallac/Wizard 1470) with 85% efficiency. The half maximal inhibitory concentration (IC_{50}) was determined using GraphPad Prism 5.0, and the inhibition constant (K_i) was calculated using the Cheng-Prusoff equation:[48] $K_i = IC_{50}/(1 + [L]/K_d)$, where [L] is the concentration of [^{125}I]IMPY used in the assay, and K_d is the dissociation constant of IMPY. The K_i value of IMPY was assessed under the same conditions as a control.

The Stability Testing of 3b and 3c upon Incubated with Mice Plasma. To validate the stability of the probes, the following procedures were used. Blood was drawn from normal ICR mice (five weeks, male), and the plasma was separated by centrifugation and stored at -80 °C. Step 1: To 500 μL mice plasma was added 50 μL **3b** or **3c** in ethanol (1 μM) in a 5 mL glass tube, and the mixture was incubated at 37 °C for 30/60 min. Step 2: After 30/60 min, the mixture was treated with 300 μL acetonitrile and filtered by flash nylon membrane (0.22 μm); the filtrates and the mice plasma (as blank control) were treated by the same method twice. Step 3: The filtrates were subjected to HPLC analysis, and the spectra were recorded using acetonitrile: water = 80%: 20% with a flow rate of 1 mL/min. The retention time and purity of **3b** and **3c** were shown in Figure S8 in Supporting Information.

BBB Penetration and Blood Clearance Rate Determination. To intuitively compare the brain uptake of the probes, ICR mice (22-24 g, 5 weeks, male) were sacrificed at 2 min after i.v. injection of the probes (2 mg/Kg, 45% DMSO and 55% propylene glycol, 50 μL), and brain samples were removed. Pictures of the brains were obtained under both visible light and UV light (365 nm). The brains of ICR mice were also removed directly as controls (Figure S9 in Supporting Information).

The brain uptake rates of **3b** (2 mg/Kg, 45% DMSO and 55% propylene glycol, 50 μL) and **3c** (0.5 mg/Kg, 45% DMSO and 55% propylene glycol, 50 μL) were analyzed by following our previously established procedures.[20] The brain uptake rates of DANIR 2c (2 mg/Kg) and CRANAD-2 (0.5 mg/Kg) were also tested in the same condition as controls.

The blood clearance rate was implemented by following the same procedures in the test of BBB penetration. In brief, ICR mice (22-24 g, 5 weeks, male, n = 3-4) were sacrificed at different time points of 2 and 60 min after i.v. injection of the probes (**3b**, 2 mg/Kg; **3c**, 0.5 mg/Kg). Blood samples were collected, anticoagulated with sodium heparin and homogenized with 1.0 mL acetonitrile. Then, the remainder homogenate was extracted with 0.5 mL acetonitrile. The extracting solution was filtered by flashing nylon membrane (0.22 μm) and dried over anhydrous sodium sulfate. After that, 100 μL of the combined acetonitrile were analyzed by HPLC. The uptake in blood was presented by % injected dose per gram (% ID/g).

Determination of the Partition Coefficient. A solution of **3b** or **3c** (5 mM) in octanol (3.0 g) was subjected to partition with octanol-saturated PBS (pH = 7.4, 3.0 g) in a test tube. The mixture was vortexed for 3 min, followed by a 5-min centrifugation at 3000 rpm. Two aliquots from the octanol (10 μL) and water (400 μL) layers were analyzed by HPLC. The log *P* value was calculated by the ratio of the peak area. The measurement was conducted in triplicate.

In Vivo Near-infrared Imaging of 3b and 3c in Nude, Tg and WT Mice. In vivo NIR imaging was performed using an IVIS Spectrum Imaging System (PerkinElmer). The excitation and emission filters used are listed in Table S4 in Supporting Information. The fluorescent light emitted from the mice was detected by a CCD camera (IS0950N5103, Andor, iKon). The acquisition and analysis of the data were performed using Living Image® 4.2.1 software.

Nude (BALB/c nude, 6 weeks, female), Tg (n = 3, C57BL6, APPswe/PSEN1, 14-19 months old, female) and age-matched wild-type mice (n = 3, C57BL6, 14-19 months old, female) were used in NIR imaging (the details of the mice used for each probe are shown in Table S4 in Supporting Information). The mice were i.v. injected with NIR probe **3b** or **3c** (0.4 mg/Kg, 10% DMSO, 90 % propylene glycol, 50 μL). Fluorescence signals of the brain were recorded at various time points (2 - 60 min) with the mice anesthetized (2.5 % isoflurane in oxygen flow, 1.5 L/min). The imaging results were quantitated by drawing an ROI around the brain region. The data were analyzed by normalizing the fluorescence intensity to the fluorescence signal of the highest values by the following method (the same method was used by Hintersteiner et al. in the NIR imaging of AOI987): for each mouse, the fluorescence signal at any given time point [F(t)] minus the background fluorescence signal before the injection [F(pre)] was divided by the fluorescence signal of the highest value [F(2 min) and F(10 min) for **3b** and **3c**, respectively]. This calculated parameter can reliably eliminate the unavoidable differences and injection capacities among individual animals.

Relative fluorescence intensity = $[F(t) - F(pre)]/[F(t`) - F(pre)]$ equation (1)

where $t \neq 0$, $t` = 2$ and 10 min for **3b** and **3c**, respectively.

Ex Vivo Fluorescence Staining of 3b and 3c to Aβ Plaques in Tg Mice Brain. A 14-month-old Tg mouse and an age-matched WT mouse were sacrificed 20 min after i.v. injection with **3b**

(0.4 mg/Kg, 10% DMSO, 90 % propylene glycol, 50 μL), and the brain samples were excised, embedded in optimum cutting temperature compound (OCT) and frozen in dry ice immediately. For fluorescence observations, the brain samples were sliced into frozen sections of 20 μm. Furthermore, the same section was co-stained with Th-S (0.125%) to confirm the distribution of Aβ plaques.

Following the same procedure, a 19-month-old Tg and an age-matched WT mouse were i.v. injected with **3c** (0.4 mg/Kg, 10% DMSO, 90 % propylene glycol, 50 μL) and sacrificed 60 min later for ex vivo fluorescence staining.

Computational Methods. All probes (**3a**-**e**) were constructed in GaussView 5.0 and optimized ground-state geometries were obtained in the water phase at the B3LYP/6-31G(d)[49-51] level of theory in Gaussian 09[52].

Docking procedures were performed using the AutoDock 4.2 software[53-55] on widely used Aβ_{1-40} fibril structures (PDB ID: 2LMO) according to the Lamarckian genetic algorithm method[56]. The optimized geometries of **3a**-**e** served as the input ligands, and the rigid protein (Aβ_{1-40} fibril) was used as the macromolecule receptor. AutoDock Tools 1.5.6[55, 57] was used in the preparation of the ligand and receptor coordinate files, and therefore, nonpolar hydrogen atoms were merged and all torsions were set to be rotatable during docking. Several studies have indicated that residues 16-KLVFFA-21 of the Aβ fibril could be the most preferential binding site for the interactions of small molecules with the fibrils.[40, 41] Thus the grid box centered on this cite was mapped with dimensions of 42 × 104 × 84 Å^3 and a grid spacing of 0.458 Å. The number of GA runs, the population size, the maximum number of evaluations, and the maximum number of generations were set to 200, 300, 2.5 × 10^7, and 27000, respectively, and default

settings were used for all other parameters. The resulting 200 conformations from docking were clustered into groups with RMSD lower than 2.0 Å.

ASSOCIATED CONTENT

Supporting Information

Additional tables and figures, ^{1}H NMR, ^{13}C NMR, MS and HRMS spectra, CIF files and extended discussion about the results of molecular docking.

AUTHOR INFORMATION

Corresponding Author

* Phone/Fax: +86-10-58808891. E-mail: cmc@bnu.edu.cn.

Author Contributions

Conceived and designed the experiments: M. Cui, H. Fu and B. Liu. Performed the experiments: H. Fu, M. Cui, L. Zhao, P. Tu and K. Zhou. Analyzed the data: H. Fu, M. Cui and L. Zhao. Contributed reagents/materials/analysis tools: M. Cui, J. Dai and B. Liu. Wrote the paper: H. Fu, M. Cui.

Notes

The authors declare no competing financial interest.

ACKNOWLEDGMENT

This work was funded by the National Natural Science Foundation of China (No. 21201019), the Beijing Municipal Natural Science Foundation (No. 7143180) and the National Science and Technology Major Projects for Major New Drugs Innovation and Development (No. 2014ZX09507007-002).

ABBREVIATIONS

AD, Alzheimer's disease; Aβ, β-amyloid; B3LYP, 3-parameter hybrid Becke exchange/Lee-Yang-Parr correlation functional; BBB, blood-brain barrier; BSA, bovine serum albumin; CAA, cerebral amyloid angiopathy; CCD, charge-coupled device; CR, Congo red; D-A, donor-acceptor; DCM, dichloromethane; DDNP, 2-(1-(6-(dimethylamino)naphthalen-2-yl)ethylidene)malononitrile; DMF, *N*,*N*'-dimethylformamide; DMSO, dimethyl sulfoxide; FDA, United States Food and Drug Administration; FDDNP, 2-(1-[6-[(2-fluoroethyl)(methyl)amino]-2-naphthyl]ethylidene); FMT, fluorescence molecular tomographic; GA, genetic algorithm; HPLC, high-performance liquid chromatography; HRMS, high-resolution mass spectrometry; ICT, internal charge transfer; IMPY, 4-(6-iodoimidazo[1,2-a]pyridin-2-yl)-*N*,*N*-dimethylaniline; i.v., intravenous; MS (EI), mass spectrometry (electron ionization); MRI, magnetic resonance imaging; J, coupling constant (in NMR spectrometry); NFTs, neurofibrillary tangles; NIR, near-infrared; NMR, nuclear magnetic resonance; OCT, optimum cutting temperature compound; PBS, phosphate buffered saline; PET, positron emission tomography; QY, quantum yield; RMSD, root-mean-square deviations; SPECT, single photon emission computed tomography; Tg, transgenic; THF, tetrahydrofuran; Th-S, thioflavin-S; Th-T, thioflavin-T; UV, ultraviolet; WT, wild-type.

REFERENCES

1. Brookmeyer, R.; Johnson, E.; Ziegler-Graham, K.; Arrighi, H. M. Forecasting the global burden of Alzheimer's disease. *Alzheimer's Dementia* **2007**, *3*, 186-191.

2. Selkoe, D. J. The origins of Alzheimer disease: a is for amyloid. *JAMA* **2000**, *283*, 1615-1617.

3. Hardy, J. The shorter amyloid cascade hypothesis. *Neurobiol. Aging* **1999**, *20*, 85; discussion 87.

4. Hardy, J.; Selkoe, D. J. The amyloid hypothesis of Alzheimer's disease: progress and problems on the road to therapeutics. *Science* **2002**, *297*, 353-356.

5. Hardy, J. A.; Higgins, G. A. Alzheimer's disease: the amyloid cascade hypothesis. *Science* **1992**, *256*, 184-185.

6. Higuchi, M.; Iwata, N.; Matsuba, Y.; Sato, K.; Sasamoto, K.; Saido, T. C. ^{19}F and ^{1}H MRI detection of amyloid beta plaques in vivo. *Nat. Neurosci.* **2005**, *8*, 527-533.

7. Schenk, D.; Barbour, R.; Dunn, W.; Gordon, G.; Grajeda, H.; Guido, T.; Hu, K.; Huang, J.; Johnson-Wood, K.; Khan, K.; Kholodenko, D.; Lee, M.; Liao, Z.; Lieberburg, I.; Motter, R.; Mutter, L.; Soriano, F.; Shopp, G.; Vasquez, N.; Vandevert, C.; Walker, S.; Wogulis, M.; Yednock, T.; Games, D.; Seubert, P. Immunization with amyloid-beta attenuates Alzheimer-disease-like pathology in the PDAPP mouse. *Nature* **1999**, *400*, 173-177.

8. Cui, M. Past and recent progress of molecular imaging probes for beta-amyloid plaques in the brain. *Curr. Med. Chem.* **2014**, *21*, 82-112.

9. Zhu, L.; Ploessl, K.; Kung, H. F. PET/SPECT imaging agents for neurodegenerative diseases. *Chem. Soc. Rev.* **2014**, *43*, 6683-6691.

10. Stuker, F.; Ripoll, J.; Rudin, M. Fluorescence molecular tomography: principles and potential for pharmaceutical research. *Pharmaceutics* **2011**, *3*, 229-274.

11. Weissleder, R.; Pittet, M. J. Imaging in the era of molecular oncology. *Nature* **2008**, *452*, 580-589.

12. Ntziachristos, V.; Tung, C.-H.; Bremer, C.; Weissleder, R. Fluorescence molecular tomography resolves protease activity in vivo. *Nat. Med.* **2002**, *8*, 757-761.

13. Gibson, E. A.; Masihzadeh, O.; Lei, T. C.; Ammar, D. A.; Kahook, M. Y. Multiphoton microscopy for ophthalmic imaging. *J. Ophthalmol.* **2011**, *2011*, 870-879.

14. Bacskai, B. J.; Kajdasz, S. T.; Christie, R. H.; Carter, C.; Games, D.; Seubert, P.; Schenk, D.; Hyman, B. T. Imaging of amyloid-beta deposits in brains of living mice permits direct observation of clearance of plaques with immunotherapy. *Nat. Med.* **2001**, *7*, 369-372.

15. Bacskai, B. J.; Hickey, G. A.; Skoch, J.; Kajdasz, S. T.; Wang, Y.; Huang, G. F.; Mathis, C. A.; Klunk, W. E.; Hyman, B. T. Four-dimensional multiphoton imaging of brain entry, amyloid binding, and clearance of an amyloid-beta ligand in transgenic mice. *Proc. Natl. Acad. Sci. U. S. A.* **2003**, *100*, 12462-12467.

16. Hintersteiner, M.; Enz, A.; Frey, P.; Jaton, A.-L.; Kinzy, W.; Kneuer, R.; Neumann, U.; Rudin, M.; Staufenbiel, M.; Stoeckli, M.; Wiederhold, K.-H.; Gremlich, H.-U. In vivo detection of amyloid-[beta] deposits by near-infrared imaging using an oxazine-derivative probe. *Nat. Biotech.* **2005**, *23*, 577-583.

17. Ran, C.; Xu, X.; Raymond, S. B.; Ferrara, B. J.; Neal, K.; Bacskai, B. J.; Medarova, Z.; Moore, A. Design, synthesis, and testing of difluoroboron-derivatized curcumins as near-infrared

probes for in vivo detection of amyloid-beta deposits. *J. Am. Chem. Soc.* **2009**, *131*, 15257-15261.

18. Zhang, X.; Tian, Y.; Li, Z.; Tian, X.; Sun, H.; Liu, H.; Moore, A.; Ran, C. Design and synthesis of curcumin analogues for in vivo fluorescence imaging and inhibiting copper-induced cross-linking of amyloid beta species in Alzheimer's disease. *J. Am. Chem. Soc.* **2013**, *135*, 16397-409.

19. Ono, M.; Watanabe, H.; Kimura, H.; Saji, H. BODIPY-based molecular probe for imaging of cerebral beta-amyloid plaques. *ACS Chem. Neurosci.* **2012**, *3*, 319-324.

20. Fu, H.; Cui, M.; Tu, P.; Pan, Z.; Liu, B. Evaluation of molecules based on the electron donor-acceptor architecture as near-infrared beta-amyloidal-targeting probes. *Chem. Commun. (Camb)* **2014**, *50*, 11875-11878.

21. Cui, M.; Ono, M.; Watanabe, H.; Kimura, H.; Liu, B.; Saji, H. Smart near-infrared fluorescence probes with donor-acceptor structure for in vivo detection of beta-amyloid deposits. *J. Am. Chem. Soc.* **2014**, *136*, 3388-3394.

22. de Silva, A. P.; Gunaratne, H. Q.; Gunnlaugsson, T.; Huxley, A. J.; McCoy, C. P.; Rademacher, J. T.; Rice, T. E. Signaling recognition events with fluorescent sensors and switches. *Chem. Rev.* **1997**, *97*, 1515-1566.

23. Alain, V.; Rédoglia, S.; Blanchard-Desce, M.; Lebus, S.; Lukaszuk, K.; Wortmann, R.; Gubler, U.; Bosshard, C.; Günter, P. Elongated push–pull diphenylpolyenes for nonlinear optics: molecular engineering of quadratic and cubic optical nonlinearities via tuning of intramolecular charge transfer. *Chem. Phys.* **1999**, *245*, 51-71.

24. Yao, L.; Zhang, S.; Wang, R.; Li, W.; Shen, F.; Yang, B.; Ma, Y. Highly efficient near-infrared organic light-emitting diode based on a butterfly-shaped donor-acceptor chromophore with strong solid-state fluorescence and a large proportion of radiative excitons. *Angew. Chem. Int. Ed. Engl.* **2014**, *53*, 2119-2123.

25. Lippert, E. Spektroskopische bestimmung des dipolmomentes aromatischer verbindungen im ersten angeregten singulettzustand. *Z. Elektrochem* **1957**, *61*, 962-975.

26. Mataga, N.; Kaifu, Y.; Koizumi, M. Solvent effects upon fluorescence spectra and the dipolemoments of excited molecules. *Bull. Chem. Soc. Jpn.* **1956**, *29*, 465-470.

27. Schwarz, F. P.; Wasik, S. P. Fluorescence measurements of benzene, naphthalene, anthracene, pyrene, fluoranthene, and benzo(e)pyrene in water. *Anal. Chem.* **1976**, *48*, 524-528.

28. Jacobson, A.; Petric, A.; Hogenkamp, D.; Sinur, A.; Barrio, J. R. 1,1-dicyano-2-[6-(dimethylamino)naphthalen-2-yl]propene (DDNP): A solvent polarity and viscosity sensitive fluorophore for fluorescence microscopy. *J. Am. Chem. Soc.* **1996**, *118*, 5572-5579.

29. Petric, A.; Johnson, S. A.; Pham, H. V.; Li, Y.; Ceh, S.; Golobic, A.; Agdeppa, E. D.; Timbol, G.; Liu, J.; Keum, G.; Satyamurthy, N.; Kepe, V.; Houk, K. N.; Barrio, J. R. Dicyanovinylnaphthalenes for neuroimaging of amyloids and relationships of electronic structures and geometries to binding affinities. *Proc. Natl. Acad. Sci. U. S. A.* **2012**, *109*, 16492-16497.

30. Bresjanac, M.; Smid, L. M.; Vovko, T. D.; Petric, A.; Barrio, J. R.; Popovic, M. Molecular-imaging probe 2-(1-[6-[(2-fluoroethyl)(methyl) amino]-2-naphthyl]ethylidene) malononitrile labels prion plaques in vitro. *J. Neurosci.* **2003**, *23*, 8029-8033.

31. Small, G. W.; Kepe, V.; Ercoli, L. M.; Siddarth, P.; Bookheimer, S. Y.; Miller, K. J.; Lavretsky, H.; Burggren, A. C.; Cole, G. M.; Vinters, H. V.; Thompson, P. M.; Huang, S. C.; Satyamurthy, N.; Phelps, M. E.; Barrio, J. R. PET of brain amyloid and tau in mild cognitive impairment. *N. Engl. J. Med.* **2006**, *355*, 2652-2663.

32. Cai, L.; Innis, R. B.; Pike, V. W. Radioligand development for PET imaging of beta-amyloid (Abeta)--current status. *Curr. Med. Chem.* **2007**, *14*, 19-52.

33. Cui, M.; Ono, M.; Kimura, H.; Kawashima, H.; Liu, B. L.; Saji, H. Radioiodinated benzimidazole derivatives as single photon emission computed tomography probes for imaging of β-amyloid plaques in Alzheimer's disease. *Nucl. Med. Biol.* **2011**, *38*, 313-320.

34. Blanchard-Desce, M.; Wortmann, R.; Lebus, S.; Lehn, J.-M.; Krämer, P. Intramolecular charge transfer in elongated donor-acceptor conjugated polyenes. *Chem. Phys. Lett.* **1995**, *243*, 526-532.

35. Haupts, U.; Rudiger, M.; Ashman, S.; Turconi, S.; Bingham, R.; Wharton, C.; Hutchinson, J.; Carey, C.; Moore, K. J.; Pope, A. J. Single-molecule detection technologies in miniaturized high-throughput screening: fluorescence intensity distribution analysis. *J. Biomol. Screen.* **2003**, *8*, 19-33.

36. Kumar-Singh, S.; Pirici, D.; McGowan, E.; Serneels, S.; Ceuterick, C.; Hardy, J.; Duff, K.; Dickson, D.; Van Broeckhoven, C. Dense-core plaques in Tg2576 and PSAPP mouse models of Alzheimer's disease are centered on vessel walls. *Am. J. Pathol.* **2005**, *167*, 527-543.

37. Rodriguez-Rodriguez, C.; Rimola, A.; Rodriguez-Santiago, L.; Ugliengo, P.; Alvarez-Larena, A.; Gutierrez-de-Teran, H.; Sodupe, M.; Gonzalez-Duarte, P. Crystal structure of

thioflavin-T and its binding to amyloid fibrils: insights at the molecular level. *Chem. Commun. (Camb)* **2010**, *46*, 1156-1158.

38. Wu, C.; Scott, J.; Shea, J. E. Binding of Congo red to amyloid protofibrils of the Alzheimer Abeta(9-40) peptide probed by molecular dynamics simulations. *Biophys. J.* **2012**, *103*, 550-557.

39. Wu, C.; Wang, Z.; Lei, H.; Zhang, W.; Duan, Y. Dual binding modes of Congo red to amyloid protofibril surface observed in molecular dynamics simulations. *J. Am. Chem. Soc.* **2007**, *129*, 1225-1232.

40. Cook, N. P.; Ozbil, M.; Katsampes, C.; Prabhakar, R.; Marti, A. A. Unraveling the photoluminescence response of light-switching ruthenium(II) complexes bound to amyloid-beta. *J. Am. Chem. Soc.* **2013**, *135*, 10810-10816.

41. Yang, Y.; Cui, M.; Zhang, X.; Dai, J.; Zhang, Z.; Lin, C.; Guo, Y.; Liu, B. Radioiodinated benzyloxybenzene derivatives: a class of flexible ligands target to beta-amyloid plaques in Alzheimer's brains. *J. Med. Chem.* **2014**, *57*, 6030-6042.

42. Fandrich, M.; Schmidt, M.; Grigorieff, N. Recent progress in understanding Alzheimer's beta-amyloid structures. *Trends Biochem. Sci.* **2011**, *36*, 338-345.

43. Hickson, J. In vivo optical imaging: preclinical applications and considerations. *Urol. Oncol.* **2009**, *27*, 295-297.

44. Li, Z.; Cui, M.; Dai, J.; Wang, X.; Yu, P.; Yang, Y.; Jia, J.; Fu, H.; Ono, M.; Jia, H.; Saji, H.; Liu, B. Novel cyclopentadienyl tricarbonyl complexes of (99m)Tc mimicking chalcone as

potential single-photon emission computed tomography imaging probes for beta-amyloid plaques in brain. *J. Med. Chem.* **2013**, *56*, 471-482.

45. Olmsted, J. Calorimetric determinations of absolute fluorescence quantum yields. *J. Phys. Chem.* **1979**, *83*, 2581-2584.

46. Sheldrick, G. M. SHELXL-97, *Program for the Refinement of Crystal Structure*; University of Göttingen: Germany, 1997.

47. Qu, W. C.; Kung, M. P.; Hou, C.; Benedum, T. E.; Kung, H. F. Novel styrylpyridines as probes for SPECT imaging of amyloid plaques. *J. Med. Chem.* **2007**, *50*, 2157-2165.

48. Cheng, Y.; Prusoff, W. H. Relationship between the inhibition constant (K1) and the concentration of inhibitor which causes 50 per cent inhibition (I50) of an enzymatic reaction. *Biochem. Pharmacol.* **1973**, *22*, 3099-3108.

49. Becke, A. D. Density ‐ functional thermochemistry. III. The role of exact exchange. *J. Chem. Phys.* **1993**, *98*, 5648-5652.

50. Dobbs, K. D.; Hehre, W. J. Molecular orbital theory of the properties of inorganic and organometallic compounds. 6. Extended basis sets for second-row transition metals. *J. Comput. Chem.* **1987**, *8*, 880-893.

51. Stephens, P. J.; Devlin, F. J.; Chabalowski, C. F.; Frisch, M. J. Ab initio calculation of vibrational absorption and circular dichroism spectra using density functional force fields. *J. Phys. Chem.* **1994**, *98*, 11623-11627.

52. Frisch, M. J.; Trucks, G. W.; Schlegel, H. B.; Scuseria, G. E.; Robb, M. A.; Cheeseman, J. R.; Scalmani, G.; Barone, V.; Mennucci, B.; Petersson, G. A.; Nakatsuji, H.; Caricato, M.; Li, X.; Hratchian, H. P.; Izmaylov, A. F.; Bloino, J.; Zheng, G.; Sonnenberg, J. L.; Hada, M.; Ehara, M.; Toyota, K.; Fukuda, R.; Hasegawa, J.; Ishida, M.; Nakajima, T.; Honda, Y.; Kitao, O.; Nakai, H.; Vreven, T.; Montgomery, J. A., Jr.; Peralta, J. E.; Ogliaro, F.; Bearpark, M.; Heyd, J. J.; Brothers, E.; Kudin, K. N.; Staroverov, V. N.; Keith, T.; Kobayashi, R.; Normand, J.; Raghavachari, K.; Rendell, A.; Burant, J. C.; Iyengar, S. S.; Tomasi, J.; Cossi, M.; Rega, N.; Millam, J. M.; Klene, M.; Knox, J. E.; Cross, J. B.; Bakken, V.; Adamo, C.; Jaramillo, J.; Gomperts, R.; Stratmann, R. E.; Yazyev, O.; Austin, A. J.; Cammi, R.; Pomelli, C.; Ochterski, J. W.; Martin, R. L.; Morokuma, K.; Zakrzewski, V. G.; Voth, G. A.; Salvador, P.; Dannenberg, J. J.; Dapprich, S.; Daniels, A. D.; Farkas, O.; Foresman, J. B.; Ortiz, J. V.; Cioslowski, J.; Fox, D. J. Gaussian 09, Revision B.01; Gaussian, Inc.: Wallingford CT, 2010.

53. Cosconati, S.; Forli, S.; Perryman, A. L.; Harris, R.; Goodsell, D. S.; Olson, A. J. Virtual screening with AutoDock: theory and practice. *Expert Opin. Drug Discovery* **2010**, *5*, 597-607.

54. Forli, S.; Olson, A. J. A force field with discrete displaceable waters and desolvation entropy for hydrated ligand docking. *J. Med. Chem.* **2012**, *55*, 623-638.

55. Morris, G. M.; Huey, R.; Lindstrom, W.; Sanner, M. F.; Belew, R. K.; Goodsell, D. S.; Olson, A. J. AutoDock4 and AutoDockTools4: automated docking with selective receptor flexibility. *J. Comput. Chem.* **2009**, *30*, 2785-2791.

56. Morris, G. M.; Goodsell, D. S.; Halliday, R. S.; Huey, R.; Hart, W. E.; Belew, R. K.; Olson, A. J. Automated docking using a Lamarckian genetic algorithm and an empirical binding free energy function. *J. Comput. Chem.* **1998**, *19*, 1639-1662.

57. Sanner, M. F. Python: a programming language for software integration and development. *J. Mol. Graphics Modell.* **1999**, *17*, 57-61.

Table of Contents Graphic

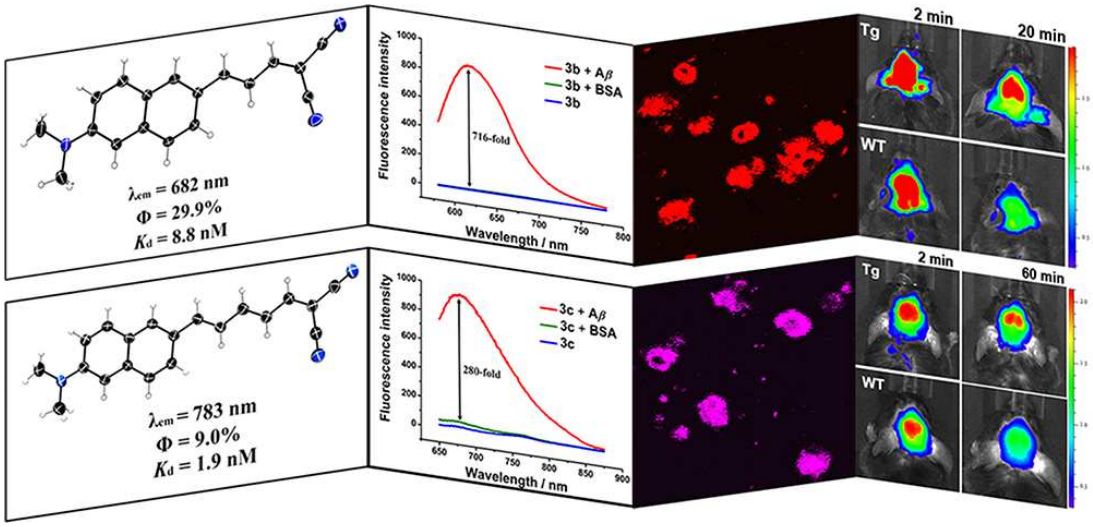

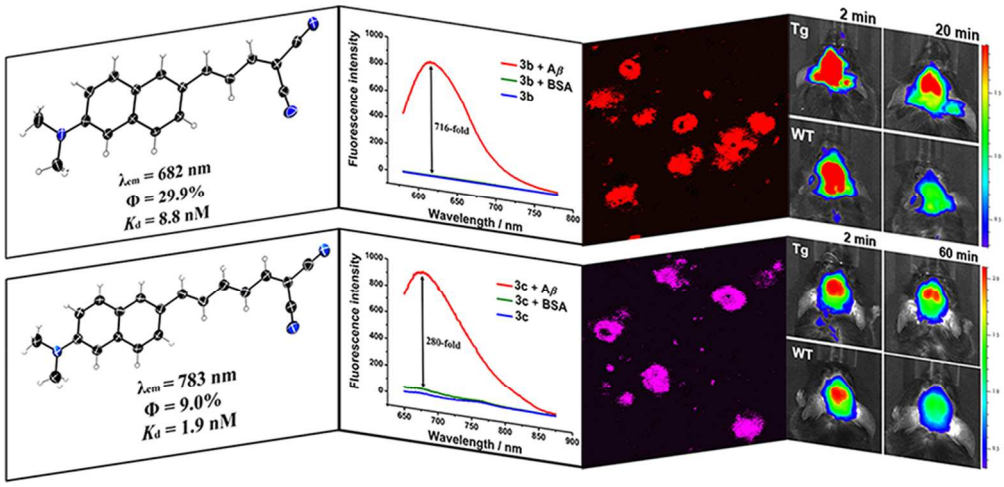

84x40mm (300 x 300 DPI)

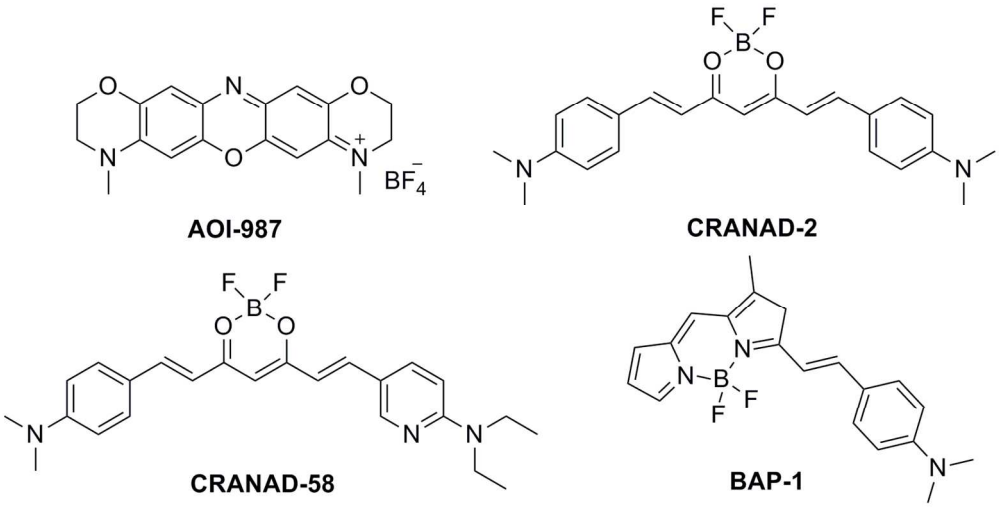

Structures of the reported NIR probes for detecting insoluble or soluble Aβ species.
140x70mm (300 x 300 DPI)

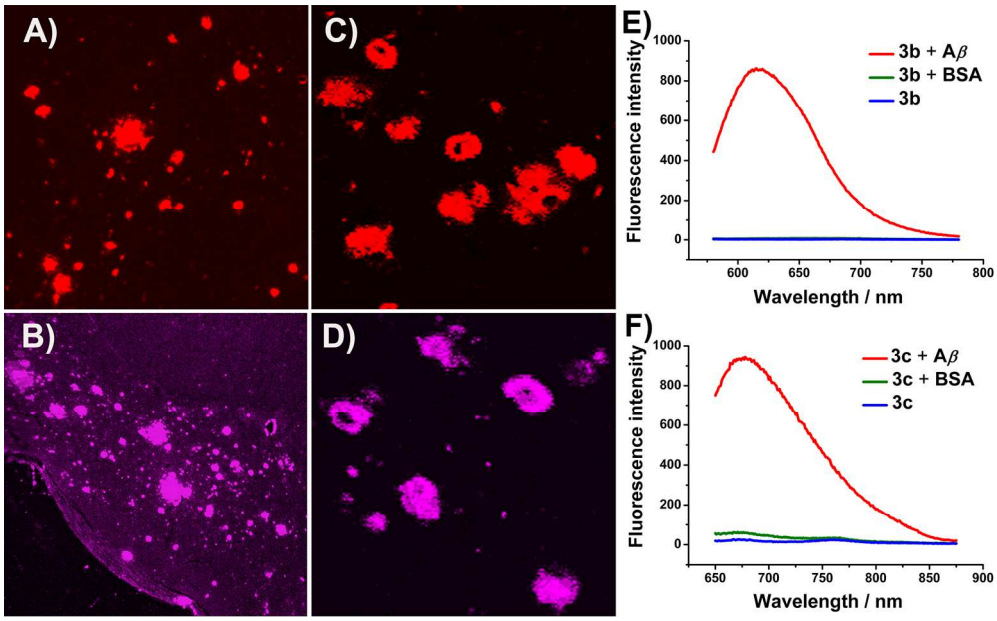

(A-D) Histological staining of brain slices from Tg mice (A and B, magnification: 10×) and an AD patient (C and D, magnification: 10×). A) and C), B) and D) were stained by 3b and 3c, respectively. (E and F) Emission wavelengths of 3b (E) and 3c (F) upon binding with Aβ aggregates or BSA.
169x103mm (300 x 300 DPI)

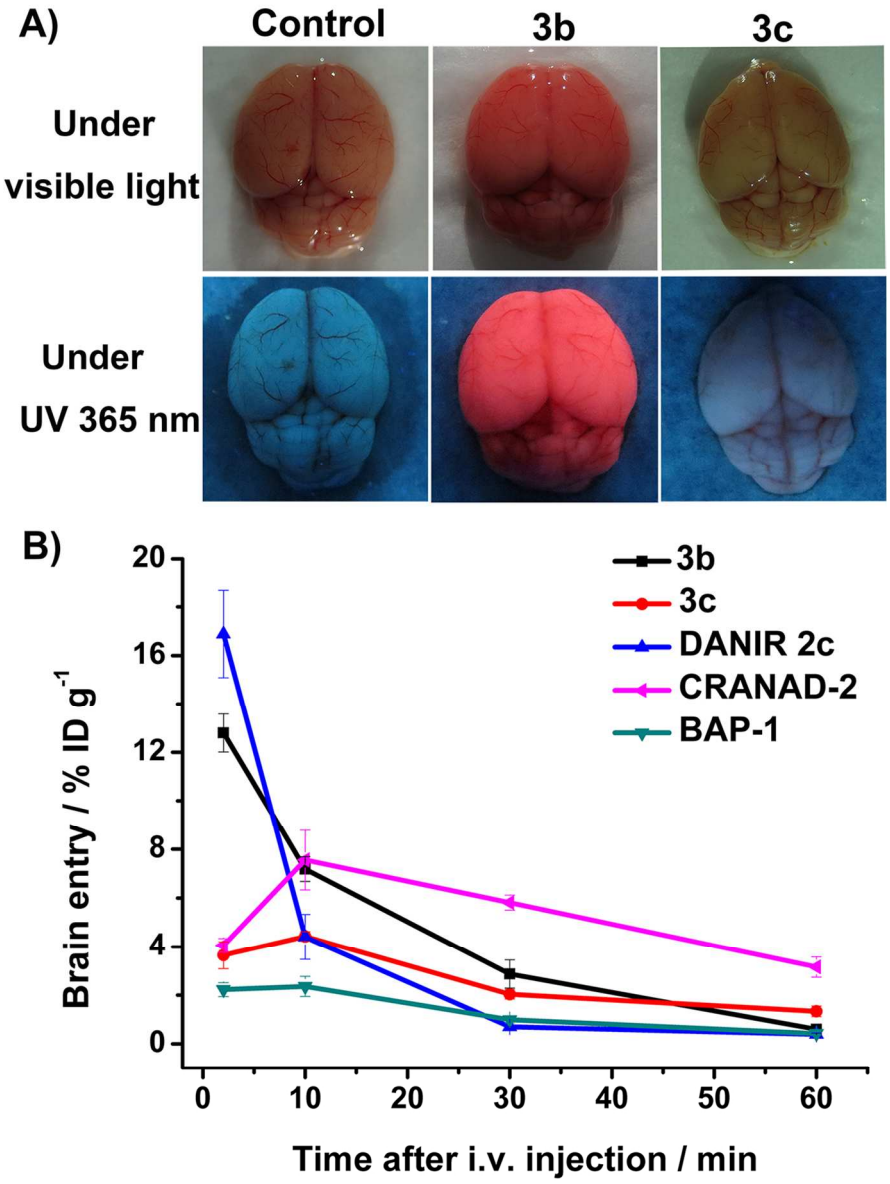

(A) Brains of ICR mice separated at 2 min after i.v. injection of 3b and 3c under visible light (top row) and UV light (365 nm, bottom row). Brains were also dissected from mice directly as a control. (B) Comparison of brain uptake of 3b, 3c, DANIR 2c, CRANAD-2 and BAP-1 in ICR mice.
108x146mm (300 x 300 DPI)

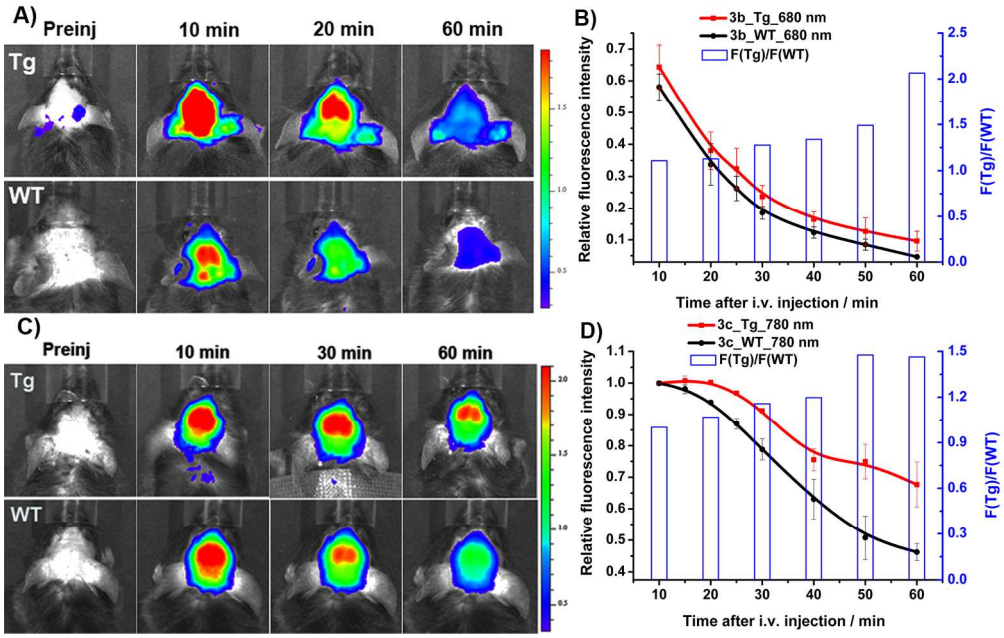

In vivo imaging of Aβ deposits by 3b and 3c. (A and C) Representative images of Tg mice (top row) and age-matched WT ones (bottom row) at selected time points before and after i.v. injection of 3b (A) and 3c (C). (B and D) Relative fluorescence intensity in the brain compartments of Tg mice (red line) and WT mice (black line) after i.v. injection of 3b (B) and 3c (D). The differences of the fluorescence signals between Tg and WT mice were also illustrated by the values of F(Tg)/F(WT) (right Y axis). The fluorescence signals of 3b and 3c were recorded at 680 (A and B) and 780 nm (C and D), respectively.
169x107mm (300 x 300 DPI)

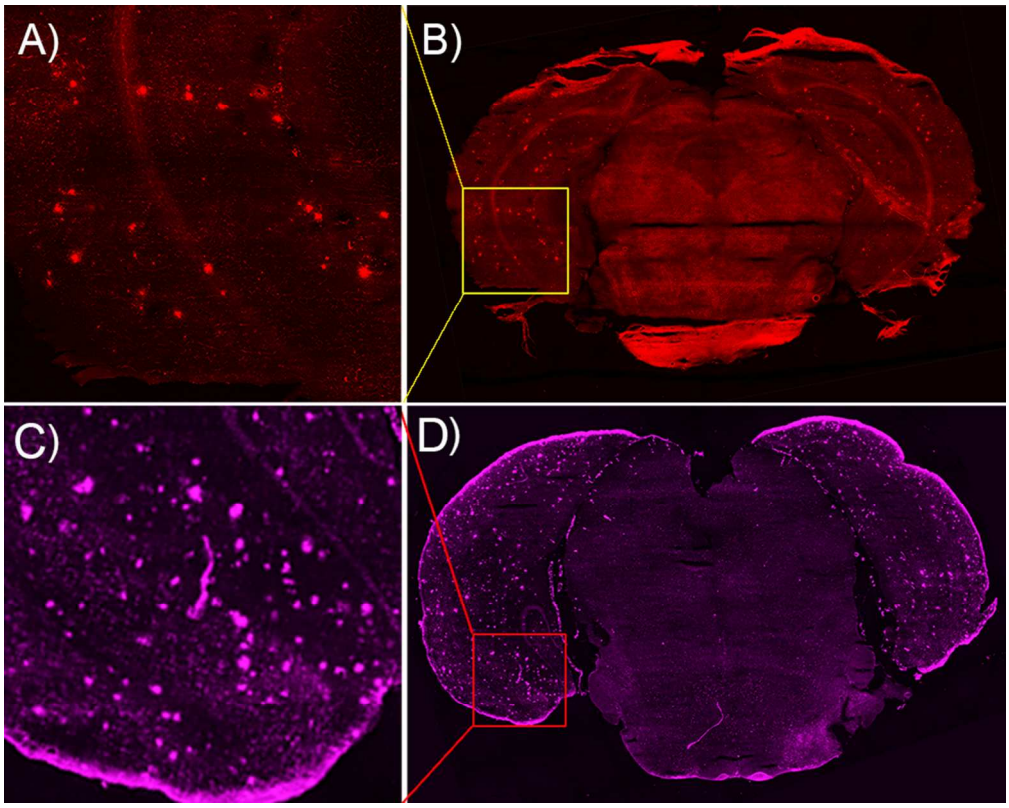

Ex vivo histology results of brain slices of cortex regions of Tg mice after dosing with 3b (A and B) and 3c (E and F). (A) and (C) are partial enlarged views of homologous sections. Magnification: 10×.
166x132mm (300 x 300 DPI)

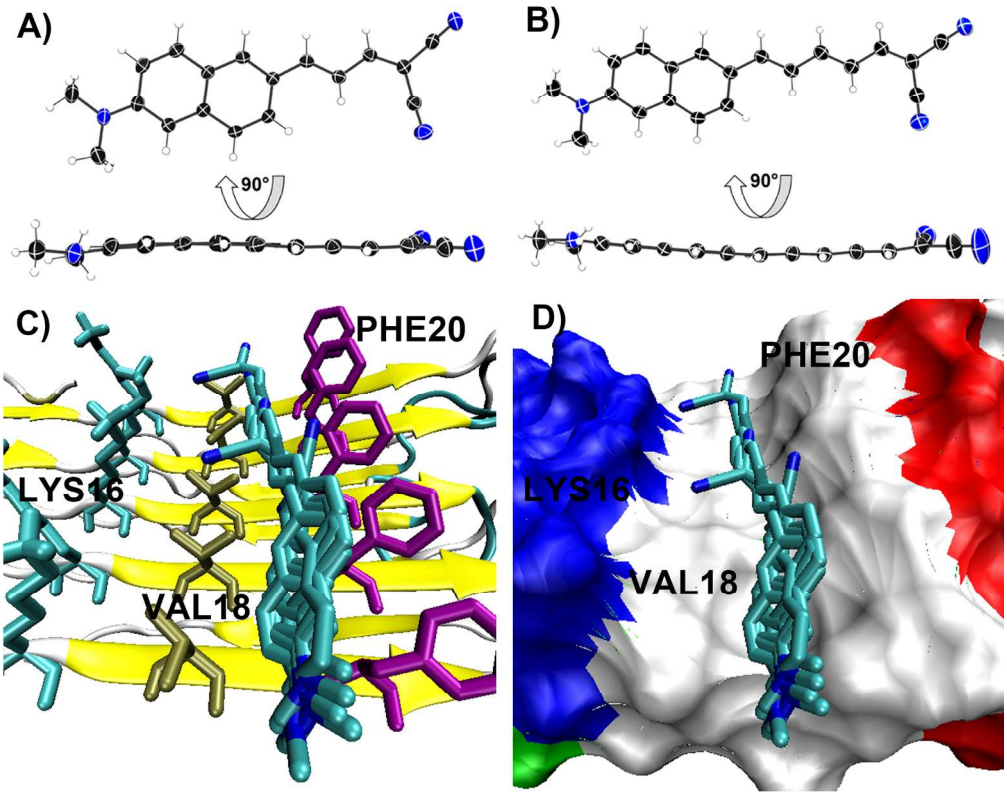

ORTEP structures of 3b (A) and 3c (B) and merged docking conformations of 3a-e (C and D). The residues of Aβ fibrils are presented in the licorice style (C) and a molecule surface representation (D).
169x134mm (300 x 300 DPI)